

**Antarctic boundary layer parametrization in a general circulation model  
1-D simulations facing summer observations at Dome C**

Vignon, Etienne; Hourdin, Frédéric; Genthon, Christophe; Gallée, Hubert; Bazile, Eric; Lefebvre, Marie Pierre; Madeleine, Jean Baptiste; Van de wiel, Bas J.H.

**DOI**

[10.1002/2017JD026802](https://doi.org/10.1002/2017JD026802)

**Publication date**

2017

**Document Version**

Final published version

**Published in**

Journal Of Geophysical Research-Atmospheres

**Citation (APA)**

Vignon, E., Hourdin, F., Genthon, C., Gallée, H., Bazile, E., Lefebvre, M. P., Madeleine, J. B., & Van de wiel, B. J. H. (2017). Antarctic boundary layer parametrization in a general circulation model: 1-D simulations facing summer observations at Dome C. *Journal Of Geophysical Research-Atmospheres*, 122(13), 6818-6843. <https://doi.org/10.1002/2017JD026802>

**Important note**

To cite this publication, please use the final published version (if applicable).  
Please check the document version above.

**Copyright**

Other than for strictly personal use, it is not permitted to download, forward or distribute the text or part of it, without the consent of the author(s) and/or copyright holder(s), unless the work is under an open content license such as Creative Commons.

**Takedown policy**

Please contact us and provide details if you believe this document breaches copyrights.  
We will remove access to the work immediately and investigate your claim.

## RESEARCH ARTICLE

10.1002/2017JD026802

## Key Points:

- One-dimensional GABLS4 simulations of a diurnal cycle of the boundary layer at Dome C, Antarctic Plateau, with the LMDZ general circulation model
- Evaluation of state-of-the-art parametrizations of turbulent mixing and of snow surface parameters
- Identification of critical aspects that needs to be verified in a GCM to correctly represent the summertime ABL over the Antarctic Plateau

## Supporting Information:

- Supporting Information S1
- Figure S1
- Figure S2
- Figure S3
- Text S1

## Correspondence to:

E. Vignon,  
etienne.vignon@univ-grenoble-alpes.fr

## Citation:

Vignon, E., F. Hourdin, C. Genthon, H. Gallée, E. Bazile, M.-P. Lefebvre, J.-B. Madeleine, and B. J. H. Van de Wiel (2017), Antarctic boundary layer parametrization in a general circulation model: 1-D simulations facing summer observations at Dome C, *J. Geophys. Res. Atmos.*, 122, 6818–6843, doi:10.1002/2017JD026802.

Received 16 MAR 2017

Accepted 6 JUN 2017

Accepted article online 9 JUN 2017

Published online 8 JUL 2017

## Antarctic boundary layer parametrization in a general circulation model: 1-D simulations facing summer observations at Dome C

Etienne Vignon<sup>1</sup> , Frédéric Hourdin<sup>2</sup>, Christophe Genthon<sup>1</sup>, Hubert Gallée<sup>1</sup> , Eric Bazile<sup>3</sup> , Marie-Pierre Lefebvre<sup>2</sup>, Jean-Baptiste Madeleine<sup>2,4</sup>, and Bas J. H. Van de Wiel<sup>5</sup>

<sup>1</sup>Université Grenoble Alpes CNRS IRD, IGE, Grenoble, France, <sup>2</sup>CNRS, UMR 8539, Laboratoire de Météorologie Dynamique (IPSL), Paris, France, <sup>3</sup>CNRM-GAME, Toulouse, France, <sup>4</sup>Sorbonne Universités, UPMC Univ Paris 06, UMR 8539, Laboratoire de Météorologie Dynamique (IPSL), Paris, France, <sup>5</sup>Faculty of Civil Engineering and Geosciences, Department of Geoscience and Remote Sensing, Delft University of Technology, Delft, Netherlands

**Abstract** The parametrization of the atmospheric boundary layer (ABL) is critical over the Antarctic Plateau for climate modelling since it affects the climatological temperature inversion and the negatively buoyant near-surface flow over the ice-sheet. This study challenges state-of-the-art parametrizations used in general circulation models to represent the clear-sky summertime diurnal cycle of the ABL at Dome C, Antarctic Plateau. The Laboratoire de Météorologie Dynamique-Zoom model is run in a 1-D configuration on the fourth Global Energy and Water Cycle Exchanges Project Atmospheric Boundary Layers Study case. Simulations are analyzed and compared to observations, giving insights into the sensitivity of one model that participates to the intercomparison exercise. Snow albedo and thermal inertia are calibrated leading to better surface temperatures. Using the so-called “thermal plume model” improves the momentum mixing in the diurnal ABL. In stable conditions, four turbulence schemes are tested. Best simulations are those in which the turbulence cuts off above 35 m in the middle of the night, highlighting the contribution of the longwave radiation in the ABL heat budget. However, the nocturnal surface layer is not stable enough to distinguish between surface fluxes computed with different stability functions. The absence of subsidence in the forcings and an underestimation of downward longwave radiation are identified to be likely responsible for a cold bias in the nocturnal ABL. Apart from model-specific improvements, the paper clarifies on which are the critical aspects to improve in general circulation models to correctly represent the summertime ABL over the Antarctic Plateau.

### 1. Introduction

Near-surface air cooling over the Antarctic Plateau exerts a significant control on the continental atmospheric circulation and on the Southern Hemisphere circulation [e.g., King and Turner, 1997]. Indeed, the negative surface radiative energy budget leads to a cooling of the air near the surface [Connolley, 1996; Hudson and Brandt, 2005] and prevailing atmospheric boundary layers (ABLs) that are stably stratified. The subsequent cold and dense near-surface flow feeds the katabatic winds that blow down the coastal slopes of the continent [Parish and Bromwich, 1987] and partially drive the meridional polar cells [James, 1989]. In a general circulation model (GCM), the way the surface-atmosphere heat exchanges are parametrized over the Antarctic Plateau is thus critical for the representation of the Southern Hemisphere circulation at high latitudes.

Modelling the near-surface turbulent exchanges over the Antarctic Plateau is challenging, first and foremost because the stable ABL over the Antarctic Plateau is often as shallow as a few tens of meters or even a few meters [e.g., King, 1990; Pietroni et al., 2012]. Correct representation of the near-surface turbulent processes thus requires a very fine vertical resolution in the first meters of the atmosphere to obtain reasonable calculations of the turbulent fluxes [Cassano et al., 2001; Vignon et al., 2016]. In addition to resolution issues, the physical parametrizations currently implemented in climate and weather forecast models have often not been developed for such extreme conditions. King et al. [2001] showed that the choice of the parametrization of surface and boundary layer turbulent heat fluxes in stable conditions significantly affects the representation of the Antarctic climate in the Hadley Centre climate model. In fact, using parametrizations with stability functions that sharply decrease with increasing stability led to stronger katabatic winds and enhanced cooling

of the Antarctic coastal waters. Although the latter type of stability functions is closer to observations at Halley Antarctic station [King and Connolley, 1997], they induce mechanical decouplings between the surface and the atmosphere over large parts of East Antarctica, as evidenced by extremely strong near-surface temperature inversions. Using in situ observations along a 45 m tower, Vignon *et al.* [2017] showed that a mechanical decoupling between the surface and the atmosphere occurs very frequently at Dome C, East Antarctic Plateau, sometimes resulting in temperature inversions greater than 25 K between 10 m and the surface.

Beyond Antarctica, the sensitivity of climate modelling to stable ABL parametrization was shown to be critical in other regions of the world. This is for instance the case, over the western parts of the North Atlantic and North Pacific oceans where persistent stable ABL form in summer [King *et al.*, 2007], but also in the Arctic [Viterbo *et al.*, 1999; Sterk *et al.*, 2013; Holtslag *et al.*, 2013; Sterk *et al.*, 2015, 2016]. An improved representation of the stable ABL in climate and weather forecast models calls not only for a better understanding of the physical mixing processes near the surface particularly in very stable conditions [e.g., Mahrt, 2014; Holtslag *et al.*, 2013] but also for a better understanding of the subgrid parametrization itself [Mahrt, 1987; Sandu *et al.*, 2013]. In a bid to improve the representation of the stable ABL in weather forecast and climate models, single column models and large eddy simulations (LES) intercomparisons were conducted in the framework of the Global Energy and Water Cycle Exchanges Project Atmospheric Boundary Layer Study (GABLS) [Holtslag, 2006; Holtslag *et al.*, 2011]. One of the main conclusions of the first three GABLS intercomparison cases is that weather forecast models simulate stable ABLs that are too deep and in which the surface drag is too strong, the low-level jets are excessively eroded and the wind veering with height is underestimated [Cuxart *et al.*, 2006; Svensson *et al.*, 2011; Bosveld *et al.*, 2014; Holtslag *et al.*, 2013]. In weather forecast models, enhanced mixing of heat in stable conditions is often maintained to prevent runaway surface cooling and unrealistically strong weather systems [Sandu *et al.*, 2013], but excessive turbulent fluxes in nocturnal conditions were also observed in most of GCMs that were involved in the Coupled Model Intercomparison Project 5 (CMIP5) in Svensson and Lindvall [2015]. While the first three GABLS experiments dealt with relatively weakly stable ABL, a fourth GABLS experiment was set up over Dome C, Antarctica, where very stable ABL frequently occurs. This fourth GABLS case consists in the comparison of single column models, LES, and observations during a clear-sky summer diurnal cycle [Bazile *et al.*, 2014, 2015]. The alternation of a shallow and strongly stratified nocturnal ABL with convection during daytime constitutes a critical challenge for the atmospheric models, pushing physical parametrizations to their limits.

The aim of this study is to challenge various formulations of the parametrization of the turbulent mixing in GCMs to represent the clear-sky summertime ABL over the Antarctic Plateau. We use the 1-D version of the Laboratoire de Météorologie Dynamique-Zoom (LMDZ) model, the atmospheric component of the IPSL Earth System model [Dufresne *et al.*, 2013], and compare GABLS4 simulations with in situ observations at Dome C. Complementary to the GABLS4 models intercomparison, the study provides further insight into the sensitivity of one particular GCM that participates in the 1-D models intercomparison exercise. Besides providing an excellent test for the specific physical parametrizations in LMDZ, the present work also gives more general hints for future developments for the representation of polar regions in GCMs.

The paper is structured as follows. Section 2 briefly reminds the climatology and the meteorological measurements at Dome C. Section 3 presents the LMDZ model and describes the relevant physical parametrizations. Section 4 presents the setup of the GABLS4 simulations, the results of a simulation that uses the standard configuration of the model, and the setup of a control simulation with adapted surface parameters and vertical grid. Section 5 then shows the results of the sensitivity analysis to turbulent mixing parametrizations. Section 6 discusses experiments with modified model forcings. Finally, section 7 presents our conclusions.

## 2. Climatological Settings and Meteorological Observations

### 2.1. Summer Climate at Dome C and the GABLS4 Case

Dome C is located in the eastern part of the high Antarctic Plateau (75°06'S, 123°20'E; 3233 m a.s.l.; local time = UTC + 8 h) where the French-Italian station Concordia has been set up. The landscape consists of a homogeneous snow desert, with no discernible slope (less than 1‰). The snow surface is covered by 10 to 30 cm snow-eroded forms called sastrugi. The sky is predominantly clear. The air is very cold and dry, with monthly mean 2 m temperature ranging from about  $-27^{\circ}\text{C}$  in austral summer to about  $-65^{\circ}\text{C}$  in the winter polar night [Genthon *et al.*, 2013]. Genthon *et al.* [2015] report a mean annual accumulation of approximately  $8 \times 10^{-2} \text{ m y}^{-1}$  of snow ( $\approx 2.7 \times 10^{-3} \text{ m w.e. y}^{-1}$ ). The "flatness" of the Dome prevents local

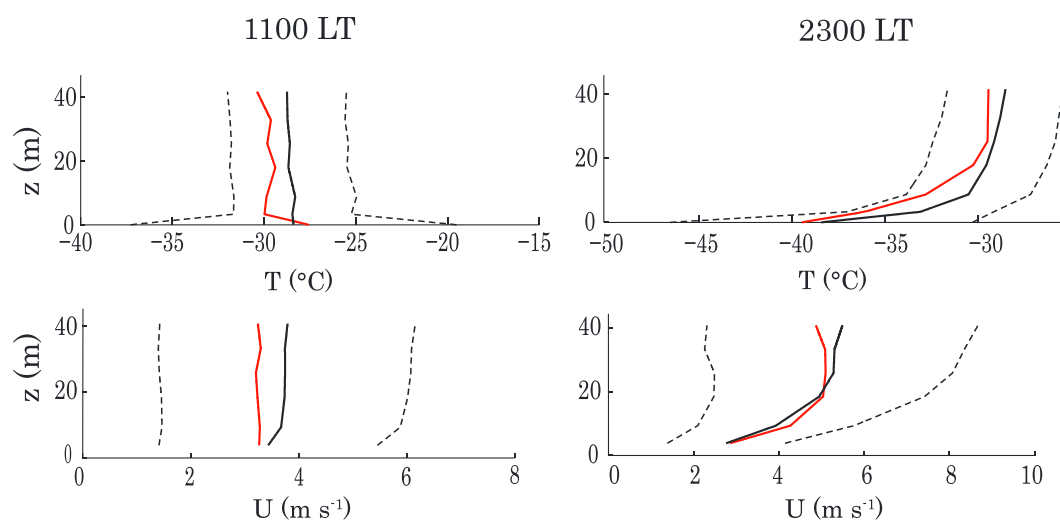


**Figure 1.** Vertical profiles of (top row) temperature and (bottom row) wind speed at (left column) 1100 LT and (right column) 2300 LT. Full black lines are the composite profiles calculated over December and January months from 2009 to 2014. Dashed black lines indicate plus or minus one standard deviation. Red lines show the profiles at 1100 on 12 December 2009 and at 2300 on 11 December 2009.

generation of katabatic winds, and the 10 m wind has a moderate annual mean speed,  $5.0 \text{ m s}^{-1}$ , and it is mostly southwesterly. Rare peaks reach  $12 \text{ m s}^{-1}$  [Argentini et al., 2014]. Few occurrences of significant wind-transported snow occur [Libois et al., 2014]. In summer (December–January–February), even though the Sun remains always above the horizon, the ABL evolves in a clear diurnal cycle. Convective activity is present during daytime [e.g., Genthon et al., 2010] referring hereafter to the time of the day when the Sun is high above the horizon and when the radiative energy budget at surface is positive. Conversely, a stable stratification sets during nighttime [Genthon et al., 2010], i.e., when the Sun is close to the horizon and when the radiative energy budget at surface is negative. The upper nocturnal ABL is often affected by an inertial oscillation with a typical period of 12.4 h. It leads to a low-level jet [Gallée et al., 2015a], peaking sometimes in the first 20 m above the ground. Sodar measurements showed that the turbulent ABL is 100–300 m deep during daytime and shallower than 50 m during nighttime [Pietroni et al., 2012; Casasanta et al., 2014]. In cloudy conditions, the amplitude of the ABL diurnal cycle is significantly reduced [Genthon et al., 2013; Gallée and Gorodetskaya, 2010].

Hereinafter, the evaluation of the 1-D version of LMDZ is made in the framework of the GABLS4 experiment [Bazile et al., 2014, 2015]. The GABLS4 single column model exercise is a 1-D simulation at Dome C for the period 11 December 2009, 0800 LT to 12 December, 2000 LT. Figure 1 shows the observation of the vertical profiles of temperature ( $T$ ) and wind speed ( $U$ ) over the first 45 m at 2300 local time (LT) on 11 December and at 1100 LT on 12 December 2009 (red lines) at Dome C. Details on the observing system are given in the next section. The profiles are close to the summertime climatological ones (solid black lines), evidencing the representativeness of the summer diurnal cycle during the GABLS4 period. The wind direction is also southwesterly and close to the climatology [Barral et al., 2014].

### 2.2. In Situ Data

In the present study, we use in situ data from the Dome C meteorological observatory. We analyze temperature and wind data obtained along a 45 m tower. We also use radiation data obtained by the Baseline Surface Radiation Network (BSRN), [Lanconelli et al., 2011] from which we retrieve the surface temperature using a

**Table 1.** Heights of Sensors on the 45 m Tower in December <sup>a</sup>

Heights of Sensors (m) on the 45 m Tower	
Temperature	3.4, 8.9, 18.0, 25.4, 32.8, 42.0
Wind	3.9, 9.4, 18.5, 25.9, 32.3, 41.7

<sup>a</sup>Heights may slightly vary with time due to snow accumulation.

surface emissivity of 0.99 [Brun *et al.*, 2012], as well as the surface albedo by calculating the ratio between the downward and upward shortwave radiations. Heights of the sensors in December 2009, i.e., during the GABLS4 period (see section 4.1) are shown in Table 1, and details on the measurements themselves can be found in Genthon *et al.* [2010, 2013]. We also use turbulence data in 2014 and 2015 estimated by eddy covariance using a Metek USA-1 sonic thermo-anemometer measurements at 3.5 m [Pietroni *et al.*, 2012; Casasanta *et al.*, 2014].

### 3. Model Description

#### 3.1. The LMDZ General Circulation Model

The model we use is an improved version of the LMDZ5B model [Hourdin *et al.*, 2013], atmospheric component of the IPSL Earth System Model (IPSL-CM5) used for climate studies and climate change projections, and in particular involved in the last CMIP5 exercise. Although initially developed for tropical and midlatitudes regions, Krinner *et al.* [1997] started to evaluate the LMDZ model over Antarctica. They proposed changes in the model physics and tuning, like a new value for the albedo for instance, to improve the representation of the polar climates. The LMDZ GCM was then used to study various aspects of the climate over Antarctica, such as tropospheric circulation [e.g., Genthon *et al.*, 2002], surface mass balance [e.g., Agosta *et al.*, 2013], oceanic forcing on the Antarctic climate [e.g., Krinner *et al.*, 2014], and transport of chemical species at high southern latitudes [e.g., Cosme *et al.*, 2005]. However, none of the studies have compared the model to in situ meteorological observations in the ABL over the Plateau.

In this study we use a version of LMDZ under development that is based on the version described in Hourdin *et al.* [2013] but contains substantial changes in the physical parametrizations. One major change is the vertical resolution: 79 levels in the new version developed for CMIP6 instead of 39 in the previous version. This new vertical discretization has been set up as a trade-off for the modelling of the stratosphere dynamics, tropospheric circulation, and ABL processes. Above Dome C, the model contains 15 levels in the first 500 m, of which three are in the first 45 m (height of the meteorological tower). We now describe the parametrizations that are expected to be critical for modelling the ABL at Dome C.

#### 3.2. Atmospheric Boundary Layer in LMDZ

In LMDZ, the parametrization of the vertical turbulent flux  $\overline{\rho w'q'}$  of a scalar  $q$  (being either the zonal or meridional wind component, the virtual potential temperature or the specific humidity) reads

$$\overline{\rho w'q'} = \rho \hat{\alpha} \hat{w} (\hat{q} - q) - \rho K_q \frac{\partial q}{\partial z} \quad (1)$$

where  $z$  is the height,  $\rho$  is the air density,  $\hat{\alpha}$  is the fraction of the horizontal surface covered by ascending plumes,  $\hat{w}$  the turbulent vertical velocity in the thermals,  $\hat{q}$  the value of  $q$  in the plume, and  $K_q$  a local turbulent diffusion coefficient.

The first term in the right-hand side of this equation corresponds to the transport by a mass flux scheme called the “thermal plume model” and described in detail in Hourdin *et al.* [2002] and Rio *et al.* [2010]. Note that this term is only active in convective conditions.

The second term in the right-hand side of equation (1) is a local turbulent diffusion term. It is parametrized using a 1.5 order closure K-gradient scheme. This scheme retains the prognostic equations for the zero-order statistics of mean wind, potential temperature and humidity, and a prognostic equation (see Appendix A) for the turbulent kinetic energy (TKE =  $1/2 \times (u'^2 + v'^2 + w'^2)$ , where  $u'$ ,  $v'$ , and  $w'$  are the turbulent fluctuations of the zonal, meridional, and vertical components of the wind, respectively) whose square root gives a turbulent velocity scale used in the formulation of the eddy diffusivity and conductivity. The version of the K-gradient scheme used in LMDZ was developed in Yamada [1983, hereafter Y83], and it is based on previous works on turbulence models for applications to the ABL in Mellor and Yamada [1974, 1982].

The expressions for the turbulent exchange coefficients for momentum  $K_m$  and for potential temperature and humidity  $K_h$  read

$$K_m = IS_m \sqrt{2 \text{TKE}} \quad (2a)$$

$$K_h = IS_h \sqrt{2 \text{TKE}} \quad (2b)$$

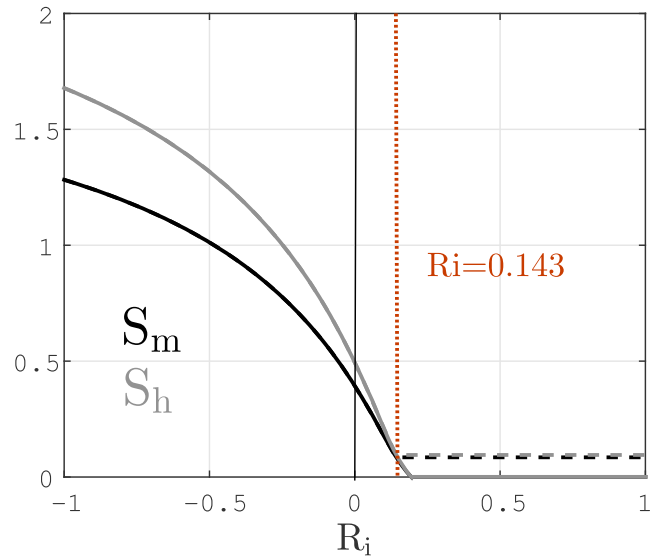


**Figure 2.**  $S_m$  and  $S_h$  versus the gradient Richardson number  $Ri$ . Solid (resp. dashed) lines show functions without (resp. with) the lower bound values prescribed in Y83.

where  $l$  is a master length scale and  $S_m$  and  $S_h$  are stability functions.  $l$  is calculated following Blackadar [1962], Deardoff [1980], and Ayotte et al. [1996] as

$$l = \min \left( l_0 \frac{\kappa z}{\kappa z + l_0}, \sqrt{\frac{\text{TKE}}{2N^2}} \right) \tag{3}$$

with  $z$  the altitude,  $\kappa = 0.4$  the Von Kármán constant, and  $N$  the Brünt Vaisala frequency.  $l_0$  is an asymptotic length scale, i.e., a limit of eddy size above the surface layer, set equal to 150 m. As an extra constraint,  $l$  is lower bounded by a minimum value  $l_{\min} = 1$  m in order to enhance the mixing in very stable conditions.  $l$  is related to the dissipation length scale  $l_\epsilon$  viz

$$l_\epsilon = \text{TKE}^{3/2} / \epsilon \tag{4}$$

$$= 2^{-3/2} \times B_1 l \tag{5}$$

where  $\epsilon$  is the TKE dissipation and  $B_1$  a constant set at 16.6 in Y83.

The stability functions  $S_m$  and  $S_h$  are semiempirical functions of the Richardson number  $Ri$ . They are plotted in Figure 2. Background values of 0.085 and 0.0952 for  $S_m$  and  $S_h$ , respectively, were introduced in Y83 for  $Ri > 0.143$  because the author pointed out that the usage of the full second-moment turbulence closure of Mellor and Yamada [1974] does not produce a clear cutoff of turbulence even at strong stability. Y83 thus retained threshold values to account for the terms in the second-moment equations that are neglected in the 1.5 order closure. The effect of such thresholds is visible in Figure 2. In the following, we will test a modified version of the current Y83 scheme with no thresholds for the  $S_m$  and  $S_h$  functions (version used in Mellor and Yamada [1982]) and with  $l_{\min} = 0$ . It will be referred to as Y83<sub>free</sub>. The discrete formulation and the numerical implementation of Y83 scheme and of the thermal plume model are detailed in Hourdin et al. [2002].

### 3.3. Alternatives for Turbulent Diffusion

After the conclusions of Cuxart et al. [2006] and Sterk et al. [2013], we can expect the modelling of the stable nocturnal ABL at Dome C to be sensitive to the choice of the turbulent scheme. That is why, in addition to the Y83 scheme, we test two alternative models for turbulent diffusion.

The TKE –  $\epsilon$  scheme from Duynkerke [1988] and that is used in the regional model MAR [Gallée and Schayes, 1994] was shown to be reasonably valid for representing the Dome C ABL in summer [Gallée et al., 2015b].

The TKE and its dissipation  $\epsilon$  are estimated with two prognostic equations, and the eddy diffusivity and the conductivity are calculated as follows:

$$K_m = c_\mu \frac{\text{TKE}^2}{\epsilon} \quad (6a)$$

$$K_h = c_\mu \frac{\text{TKE}^2}{\epsilon} Pr^{-1} \quad (6b)$$

with  $c_\mu$  a constant and  $Pr$  the turbulent Prandtl number. This method shows the advantage to circumvent the parametrization of a master length scale as in the Y83 scheme, and the prognostic equation on dissipation allows one to relate the mixing length to local sources of turbulence. However, a TKE- $\epsilon$  scheme requires the resolution of two prognostic equations rather than one, and the prognostic equation for  $\epsilon$  needs a calibration of semiempirical parameters. As underlined, for instance, by *Sukoriansky et al.* [2005], the basic TKE- $\epsilon$  scheme implies a constant Prandtl number. Several studies like *Esau and Grachev* [2007], *Zilitinkevich et al.* [2008], or *Anderson* [2009] show that the Prandtl number increases with stability probably because of the increase of the relative contribution of internal waves to the mixing. *Sukoriansky et al.* [2005] propose a spectral theory as an extension of the TKE- $\epsilon$  model that includes an parametrization of the Prandtl number accounting for stability effects. They obtain good model-observation comparisons with data from the Surface HEat Budget in the Arctic program. Following *Gallée et al.* [2015b], we thus decided to include this  $Pr$  parametrization. In the present study, the TKE- $\epsilon$  scheme was implemented in LMDZ using an implicit time integration scheme developed in *Deleersnijder* [1992].

*Zilitinkevich et al.* [2013, hereafter Z13] propose a new class of turbulence closure models for stably stratified geophysical flows. To account for the increase in turbulence anisotropy with an increase in stability, a new parametrization of turbulence anisotropy was developed. A prognostic equation of the turbulent potential energy (TPE =  $1/2 \times \left(\frac{g}{\theta N}\theta'\right)^2$ , where  $g$  is the acceleration due to gravity,  $\theta$  is the potential temperature, and  $\theta'$  is the turbulent fluctuation of the potential temperature) was also added. Accounting for TPE allows for the maintenance of turbulence by wind shear even at large  $Ri$  [*Mauritsen et al.*, 2007]. In other words, it prevents the TKE from irredeemably decaying as  $Ri$  exceeds a critical value like in common turbulence schemes that only include a TKE equation. As TPE increases, the countergradient contribution to the turbulent heat flux due to the buoyancy effect of potential temperature fluctuations increases, leading to a decrease in  $K_h$  and thus to an increase  $Pr$  with stability [*Zilitinkevich et al.*, 2007]. For this study, we have implemented in LMDZ the turbulence closure recommended for climate models (so-called the “downgradient transport model” in Z13) which is based on three prognostics equations: one for the TKE, one for the TPE, and one for  $t_\epsilon = \text{TKE}/\epsilon$ . In this closure, the eddy viscosity and conductivity read

$$K_m = 2C_\tau t_\epsilon A_z \text{TKE} \quad (7a)$$

$$K_h = 2C_F t_\epsilon A_z \text{TKE} \left(1 - \frac{C_\theta \text{TPE}}{A_z \text{TKE}}\right) \quad (7b)$$

$C_\tau$ ,  $C_F$ , and  $C_\theta$  being numerical constants equal to 0.2, 0.25 and 0.105 respectively [*Zilitinkevich et al.*, 2013].  $A_z = \text{TKE}_z/\text{TKE}$  with  $\text{TKE}_z$  the vertical component of TKE. Although the Z13 scheme has not been developed for moist air, this is not critical here since we perform simulations in the very dry atmosphere of the Antarctic Plateau. The Z13 system of three prognostics equations has been implemented with a “forward-backward” numerical scheme, and it is numerically stable for time steps of a few tens of seconds, which is reasonable for 1-D simulations.

### 3.4. Surface Turbulent Fluxes

The surface turbulent fluxes are calculated with bulk formulae between the surface and the first model level. The surface wind stress  $\tau$ , the surface sensible heat flux  $H$ , and the surface latent heat flux  $L_e$  over snow read

$$\tau = \rho_1 U_*^2 = \rho C_d U_1^2 \quad (8)$$

$$H = -\rho_1 c_p C_h U_1 (\theta_{v1} - \theta_s) \quad (9)$$

$$L_e = -\rho_1 L_{\text{sub}} C_h U_1 (q_{v1} - q_{vs}) \quad (10)$$

with  $u_*$  the friction velocity;  $c_p$  the specific heat of air at constant pressure;  $L_{\text{sub}}$  the latent heat of sublimation; and  $U$ ,  $\theta_v$ , and  $q_v$  the wind speed, the virtual potential temperature, and the specific humidity respectively. The subscript 1 refers to quantities at the first model level, and the subscript  $s$  refers to surface variables. Saturation with respect to ice over snow-covered surfaces is assumed.  $C_d$  and  $C_h$  are the drag coefficients for momentum and heat respectively (we make here the usual assumption that drag coefficients for heat and moisture are equal), and they read

$$C_d = \frac{\kappa^2}{\ln(z_1/z_0)^2} \times f_m \quad (11)$$

$$C_h = \frac{\kappa^2}{\ln(z_1/z_0) \ln(z_1/z_{0t})} \times f_h \quad (12)$$

$z_1$  is the height of the first model level,  $z_0$  and  $z_{0t}$  are the roughness lengths for momentum and heat, respectively, and  $f_m$  and  $f_h$  are stability functions of the bulk Richardson number  $Ri_b$  between the first model level and the surface. The default value of  $z_0$  and  $z_{0t}$  over the Antarctic Plateau implemented in LMDZ is  $10^{-3}$  m which is the same value as in the European Center for Medium Range Weather Forecasts (ECMWF) Integrated Forecast System model [Dutra et al., 2015]. This value is close to the mean  $z_0$  value of  $5.6 \times 10^{-4}$  m found for Dome C in Vignon et al. [2016] although the latter study mentions that  $z_0$  significantly varies with wind direction due to the alignment of the sastrugi. Moreover, the ratio  $z_{0t}/z_0$  over snow-covered surfaces may vary with the near-surface flow [Andreas, 1987]. Vignon et al. [2016] suggested that atmospheric models need a dynamical parametrization of roughness lengths over Antarctica to optimize the calculation of turbulent fluxes and, furthermore, to calculate drifting snow fluxes. Hitherto, such a parametrization is not available for GCMs and we thus keep  $z_0$  and  $z_{0t}$  as constants in the present study.

The  $f_m$  and  $f_h$  functions currently implemented in LMDZ are those from Louis et al. [1982] (L82). For stable surface layers, these functions read as follows:

$$f_m = 1 / \left( 1 + 10 \frac{Ri_b}{\sqrt{1 + 5 \times Ri_b}} \right) \quad (13a)$$

$$f_h = 1 / \left( 1 + 15 \times Ri_b \sqrt{1 + 5 \times Ri_b} \right) \quad (13b)$$

They are considered as “long-tail” functions because they maintain a significant level of turbulence even at large  $Ri_b$  (see Figure 3). They were shown to be appropriate for use in atmospheric models as they empirically compensate for the unresolved variability inside a model grid box [Delage, 1997], and they prevent surface-atmosphere decouplings [McNider et al., 2012]. Cassano et al. [2001] showed that the turbulent fluxes calculation at Halley station is sensitive to the choice of the stability function in stable conditions. We therefore decided to test alternative stability functions. King and Connolley [1997] show that the Monin-Obukhov (MO) similarity functions agree reasonably well with observations at Halley station. Assuming that the roughness lengths for momentum and heat are equal and that the similarity functions for momentum and heat are identical linear functions of  $z/L$  ( $L$  being the MO length), England and McNider [1995] show that the corresponding  $f_m$  and  $f_h$  read as follows:

$$f_{m,h} \begin{cases} (1 - \beta Ri_b)^2, & Ri_b < 1/\beta \\ 0, & Ri_b \geq 1/\beta \end{cases} \quad (14a)$$

$$f_{m,h} \begin{cases} (1 - \beta Ri_b)^2, & Ri_b < 1/\beta \\ 0, & Ri_b \geq 1/\beta \end{cases} \quad (14b)$$

with  $\beta = 5$  according to King et al. [2001]. Vignon et al. [2016] show that, in stable conditions, commonly-used similarity functions for dimensionless wind shear  $\phi_m$  reasonably fit the in situ data at Dome C, while the similarity functions for dimensionless temperature gradient  $\phi_h$  become low biased as the stability increases.  $\phi_m$  and  $\phi_h$  functions are linked to  $f_m$  and  $f_h$  viz  $f_m = \phi_m^{-2}$  and  $f_h = \phi_m^{-1} \phi_h^{-1}$  [England and McNider, 1995]. Green lines in Figure 3 show that the MO-based functions of King and Connolley [1997] better fit the in situ estimations of  $f_m$  and  $f_h$  at Dome C (grey dots) than the L82 functions, consistently with results obtained at Halley. We can also notice that these functions vanish at a critical Richardson number  $1/\beta$  implying a cutoff of turbulence at large  $Ri_b$ .

Following the ideas of Derbyshire [1999], King et al. [2001] (K01) found a trade-off between long-tail functions and the MO functions that lead to improved simulations of surface fluxes over Antarctica.

$$f_m = f_h = \begin{cases} (1 - \beta_2 Ri_b)^2, & Ri_b < \frac{1}{2\beta_2} \\ 0.0625(\beta_2 / Ri_b)^2, & Ri_b \geq \frac{1}{2\beta_2} \end{cases} \quad (15a)$$

$$f_m = f_h = \begin{cases} (1 - \beta_2 Ri_b)^2, & Ri_b < \frac{1}{2\beta_2} \\ 0.0625(\beta_2 / Ri_b)^2, & Ri_b \geq \frac{1}{2\beta_2} \end{cases} \quad (15b)$$

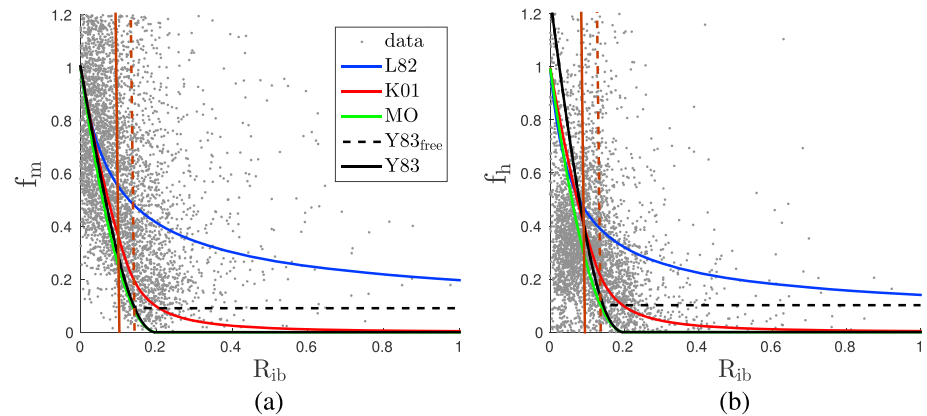


**Figure 3.** (a)  $f_m$  and (b)  $f_h$  stability functions in the surface layer versus the bulk Richardson number.  $f_m$  and  $f_h$  data estimated from observations (grey dots) were obtained from a data set of dimensionless wind shear  $\phi_m$  and temperature gradient  $\phi_h$  calculated from near-surface wind, temperature, and turbulence measurements in January, February, November, and December 2014 and 2015, with the same method as in Vignon *et al.* [2016]. We then used the relations  $f_m = \phi_m^{-2}$  and  $f_h = \phi_m^{-1} \phi_h^{-1}$  (see text for details). The L82 (blue line), K01 (red line), and MO (green line) schemes are plotted as well as the first-order-like stability functions of the Y83 (solid black line) and Y83<sub>free</sub> (dashed black line) (see Appendix B). The brown (resp. dashed) solid lines indicate  $Ri_b = 0.1$  (resp.  $Ri_b = 0.14$ ), i.e., the maximum value reached in the simulations with a first model level at 3m (resp. at 8m); see section 5.3.

with  $\beta_2 = 4$ . Figure 3 shows that MO functions and K01 (red curves) functions are closer to the first-order-like stability functions of the Y83 and Y83<sub>free</sub> schemes [Cuxart *et al.*, 2006] (see Appendix B for details) compared to the L82 functions. MO functions and the K01 functions in the surface layer are thus more consistent with the standard turbulent diffusion scheme in LMDZ. One can further point out in Figure 3 that the K01 functions show the best comparison with both  $f_m$  and  $f_h$  in situ data (grey dots). The sensitivity to the choice of stability functions in the first model layer in stable conditions is assessed in section 5.3.

The turbulence schemes as well as the surface drag schemes are listed in Table 2.

### 3.5. Albedo and Snow Thermal Inertia

In the standard LMDZ version, snow albedo over “land ice” surfaces (alb) is a constant fixed to 0.77 for both visible and near-infrared spectra. This value is in the bottom part of the range for the Antarctic Plateau [e.g., Grenfell and Warren, 1994] and particularly for Dome C [King *et al.*, 2006]. It was tuned in the version of the model used for previous CMIP exercises to compensate for a deficit in longwave downward radiation at the surface. We reconsider the albedo value for the GABLS4 case in section 4.4.

The heat transfer in the snow is parametrized as a conductive process with a fixed thermal inertia  $I = \sqrt{\lambda_s \rho_s C_s}$ ,  $\lambda_s$ ,  $\rho_s$ , and  $C_s$  being, respectively, the conductivity, the density, and the specific heat per unit mass of the snow. The scheme of the heat transfer in the ground is detailed in Hourdin [1992] and Ait-Mesbah *et al.* [2015].

**Table 2.** Acronyms and Specifications of the Turbulence Schemes and of the Surface Drag Coefficient Schemes Depending on the  $f_m$  and  $f_h$  Functions in Stable Conditions

Acronym	Specification
<i>Turbulence Scheme</i>	
Y83	1.5 order closure scheme from Yamada [1983]
Y83 <sub>free</sub>	Yamada [1983] scheme, with no $S_{m,h}$ thresholds and $I_{\min} = 0$
TKE- $\epsilon$	TKE- $\epsilon$ scheme from Duynkerke [1988]
Z13	Energy-flux budget scheme from Zilitinkevich <i>et al.</i> [2013]
<i>Surface Drag Coefficient Scheme in Stable Conditions</i>	
L82	$f_{m,h}$ from Louis <i>et al.</i> [1982]
K01	$f_{m,h}$ “SHARP” functions from King <i>et al.</i> [2001] and Derbyshire [1999]
MO	$f_{m,h}$ similar to linear MO functions from England and McNider [1995]

The current vertical discretization with 11 levels enables to represent the *e*-folding damping of thermal waves with typical periods from 1800 s (first layer) to 240 y (eleventh layer).

The numerical value of the snow thermal inertia is critical, since it significantly constrains the amplitude of the diurnal temperature range [Ait-Mesbah *et al.*, 2015]. The default value of the snow thermal inertia over ice sheets in LMDZ is  $2000 \text{ J m}^{-2} \text{ K}^{-1} \text{ s}^{-1/2}$ , a typical value of pure ice. The first 20 cm of snow at Dome C, i.e., the depth that absorbs the major part of the temperature diurnal cycle, has a mean density of  $\approx 300 \text{ kg m}^{-3}$  [Libois *et al.*, 2014]. Using the thermodynamical laws in Yen [1981] at  $T = 233 \text{ K}$  leads to  $I = 321 \text{ J m}^{-2} \text{ K}^{-1} \text{ s}^{-1/2}$ . It is worth noting that the attribution of inappropriate values for surface parameters over ice sheets in LMDZ is observed in other GCMs. For instance, Dutra *et al.* [2015] revealed that in the IFS GCM over Antarctica, the snow “thermal depth” was set at 1 m. As a consequence, the thermal inertia of the snow was significantly overestimated and this prevented to capture the short time scales (to a few hours) of the surface temperature variations at the South Pole. Likewise, Scheider and Reush [2016] show that climate models among CMIP5 have biases in albedo over Antarctica up to 0.062 compared to satellite observations, leading to significant errors in the radiative energy budget at the surface.

## 4. GABLS4 LMDZ Simulations

### 4.1. GABLS4 Setup

In the GABLS4 exercise, the 1-D version of LMDZ is run during 36 h from 11 December 2009 at 0800 LT. The model is laterally forced with the geostrophic wind ( $U_{\text{geo}}$ ) and with advections of temperature and humidity. Further details on the GABLS4 setup can be found on the Web pages [http://www.umn-cnrm.fr/aladin/meshtml/GABLS4/workshop\\_tlse\\_site/Wednesday/General\\_objectives\\_EBazile.pdf](http://www.umn-cnrm.fr/aladin/meshtml/GABLS4/workshop_tlse_site/Wednesday/General_objectives_EBazile.pdf) and [http://www.umn-cnrm.fr/aladin/meshtml/GABLS4/workshop\\_tlse\\_site/Wednesday/LeMoigne\\_GABLS4.pdf](http://www.umn-cnrm.fr/aladin/meshtml/GABLS4/workshop_tlse_site/Wednesday/LeMoigne_GABLS4.pdf).

One-dimensional simulations were carried out with three different vertical grids:

1. The default 79-level grid defined for the IPSL-CM6 configuration of the IPSL coupled model that will be used for the CMIP6 exercise. The first level is at about 6.5 m above the surface, and there are three levels in the first 45 m.
2. A refined 90-level grid prescribed for the fourth stage of the GABLS4 experiment [Bazile *et al.*, 2015], with a first level at 3 m above the surface and eight levels in the first 45 m.
3. An 89-level grid identical to the 90-level one except that the first model level is at 8 m above the surface, with the first layers encompassing the two first layers of the 90-level grid.

A 30 s time step is used for all the experiments in order to ensure numerical stability of all the turbulence schemes. It is worth noting that for simulations with the Y83 turbulence scheme, all the 1-D results are consistent for time steps up to a few minutes. The radiative transfer code is called every 10 min.

One-dimensional simulations are summarized in Table 3. Numbers at the end of the names refer to the vertical grid. Further details about the simulations are given throughout the manuscript.

### 4.2. Standard Configuration of LMDZ

Figure 4 shows a comparison of simulated temperature and wind speed with observations on the meteorological tower (left) for the current standard LMDZ configuration (row “STD-79” in Table 3). In the observations (Figures 4a and 4d), we clearly see the alternation of a diurnal convective activity associated with well-mixed temperature and wind with a shallow stable nocturnal ABL (white arrows indicate when the net radiative budget at the surface reverses sign) with significant vertical gradients of temperature and wind speed up to about 20 m at midnight. At 0800 LT on the second day, the convection initiates again. During the first part of the night, we observe an acceleration of the wind down to 10 m (Figure 4d). The nocturnal wind speed then decays and accelerates again around 0500 LT above 20 m. This wind pattern is characteristic of the development of a low-level jet associated to an inertial oscillation as explained in Gallée *et al.* [2015a].

LMDZ captures relatively well the temperature and wind during daytime even though temperature is cold biased, and the wind speed during the second day is overestimated. During nighttime, the stratification of temperature and vertical wind shear is strongly underestimated and the near-surface temperature is too high. Even though a nocturnal jet is simulated, it peaks at around 75 m at 0100 LT, much higher than in the observations.

**Table 3.** Table of the 1-D GABLS4 Experiments<sup>a</sup>

Simulations	Res	$z_1$ (m)	alb	$l$ ( $J m^{-2} K^{-1} s^{-1/2}$ )	$z_0, z_{0t}$ (m)	$f_m, f_h$	$K_m, K_h$	TPM
STD-79	79	6.5	0.77	2000	$10^{-3}, 10^{-3}$	L82	Y83	Yes
Alb-79	79	6.5	0.81	2000	$10^{-3}, 10^{-3}$	L82	Y83	Yes
l-79	79	6.5	0.77	321	$10^{-3}, 10^{-3}$	L82	Y83	Yes
new-snow-79	79	6.5	0.81	321	$10^{-3}, 10^{-3}$	L82	Y83	Yes
CTRL-90	90	3	0.81	321	$10^{-3}, 10^{-4}$	K01	Y83	Yes
Y83-79	79	6.5	0.81	321	$10^{-3}, 10^{-4}$	L82	Y83	Yes
noTPM-90	90	3	0.81	321	$10^{-3}, 10^{-4}$	K01	Y83	No
noTPM-79	79	6.5	0.81	321	$10^{-3}, 10^{-4}$	K01	Y83	No
Y83 <sub>free</sub> -90	90	3	0.81	321	$10^{-3}, 10^{-4}$	K01	Y83 <sub>free</sub>	Yes
TKE-c-90	90	3	0.81	321	$10^{-3}, 10^{-4}$	K01	TKE-c	Yes
Z13-90	90	3	0.81	321	$10^{-3}, 10^{-4}$	K01	Z13	Yes
Y83 <sub>free</sub> -79	79	6.5	0.81	321	$10^{-3}, 10^{-4}$	K01	Y83 <sub>free</sub>	Yes
L82-90	90	3	0.81	321	$10^{-3}, 10^{-4}$	L82	Y83 <sub>free</sub>	Yes
K01-90	90	3	0.81	321	$10^{-3}, 10^{-4}$	K01	Y83 <sub>free</sub>	Yes
MO-90	90	3	0.81	321	$10^{-3}, 10^{-4}$	MO	Y83 <sub>free</sub>	Yes
z0h-90	90	3	0.81	321	$10^{-3}, 10^{-3}$	K01	Y83 <sub>free</sub>	Yes
z1-L82-89	89	8	0.81	321	$10^{-3}, 10^{-4}$	L82	Y83 <sub>free</sub>	Yes
z1-K01-89	89	8	0.81	321	$10^{-3}, 10^{-4}$	K01	Y83 <sub>free</sub>	Yes
z1-MO-89	89	8	0.81	321	$10^{-3}, 10^{-4}$	MO	Y83 <sub>free</sub>	Yes
z1-z0h-89	89	8	0.81	321	$10^{-3}, 10^{-4}$	K01	Y83 <sub>free</sub>	Yes

<sup>a</sup>“Res” refers to the number of levels in the vertical grid. “TPM” refers to activation of the thermal plume model.

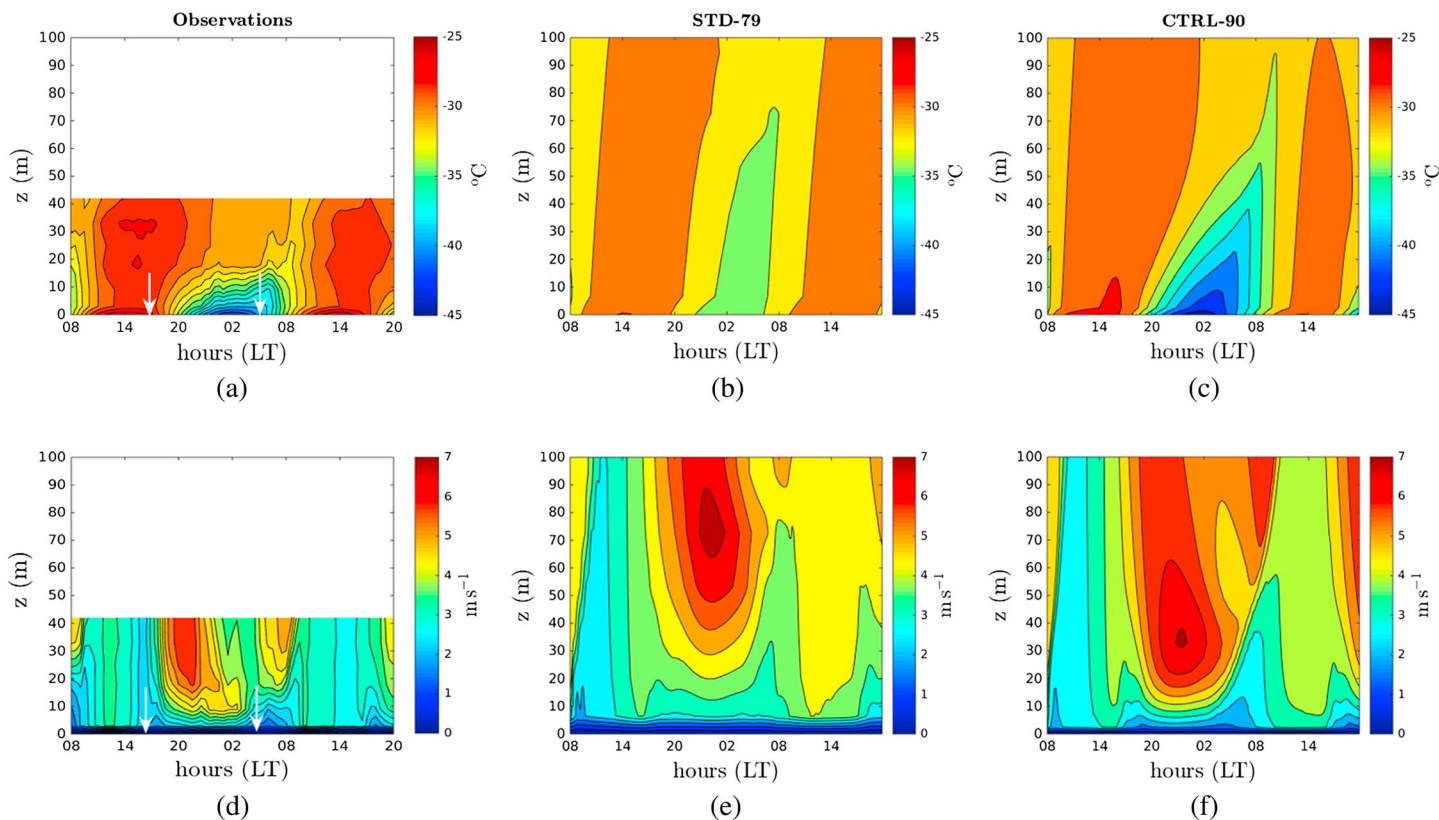


**Figure 4.** (a–c) Temperature and (d–f) wind speed in the observations (left), in the STD-79 simulation (middle), and in the CTRL-90 simulation (right). White arrows indicate times at which the net radiative budget at the surface reverses sign.

### 4.3. Adapted Snow Parameters

The major differences in the thermal structure of the ABL between the STD-79 simulation and the observations come from an inappropriate default setting of the values of the snow albedo and of the snow thermal inertia in the model. Hereafter, we explore the impact of the sole change in the snow albedo from the default 0.77 value to the observed 0.81 value (average over the GABLS4 period and recommended after the first GABLS4 workshop in Toulouse, France, [Bazile *et al.*, 2015]) and in the snow thermal inertia from the default  $2000 \text{ J m}^{-2} \text{ K}^{-1} \text{ s}^{-1/2}$  value to  $321 \text{ J m}^{-2} \text{ K}^{-1} \text{ s}^{-1/2}$  to better fit observations at Dome C. The simulation that accounts for the change in albedo (resp. thermal inertia) but keeps the original value of the snow thermal inertia (resp. albedo) is referred to as Alb-79 (resp. I-79). The simulation with both changes is referred to as new-snow-79.

In Figure 5, comparing the STD-79 (green dashed line) and the I-79 simulations (green solid line) that differ only by the prescribed value of the snow thermal inertia, one can point out that this parameter exerts a significant control on the amplitude of the diurnal cycle of the surface temperature  $T_s$  (top), of the sensible heat flux  $H$  (bottom left), and of the snow conductive heat flux  $G$ , defined positive downward (bottom right). The higher the thermal inertia, the lower the amplitude of the diurnal cycle of  $T_s$  and  $H$  and the higher the amplitude of the diurnal cycle of  $G$ . In the Alb-79 simulation with a realistic albedo but overestimated snow thermal inertia (dashed blue line), the diurnal cycle of  $T_s$  is underestimated compared to observations, with a cold bias during the “day” and a more pronounced warm bias during the “night.” Following on from the analysis of the role of the thermal inertia in the representation of the diurnal range of surface temperature in Ait-Mesbah *et al.* [2015], the asymmetry of the magnitude of the bias between daytime and nighttime can be explained as follows.

During daytime, an overestimated  $I$  leads to an overestimation of  $G$  (in magnitude) that tends to make the surface temperature cold biased. As  $\partial H / \partial(\theta_{v1} - \theta_s)$  is large (in magnitude) in convective conditions, the cold bias at the surface results in a significant underestimation of the sensible heat flux (Figure 5b) that acts to damp the cold bias at the surface.

On the other hand, during nighttime, the ABL turbulence and the surface sensible heat flux are weaker. The negative feedback in response to the higher nighttime  $G$  (in magnitude) is therefore not efficient, and the surface temperature becomes significantly warm biased.

Using a snow thermal inertia of  $I = 321 \text{ J m}^{-2} \text{ K}^{-1} \text{ s}^{-1/2}$  and a snow albedo of 0.81 in the new-snow-79 simulation (solid blue lines) leads to a much better agreement between simulated and observed  $T_s$ . Comparing the new-snow-79 simulation with the I-79, one can particularly notice the better daytime surface temperatures due to the setting of a more correct value of the albedo. However, the new-snow-79 simulation is too cold by 2 K during the night compared to the observations and this aspect is further discussed in section 6. In the new-snow-79 simulation, it is worth noting that  $H$  and  $G$  values are close to the typical values for the summer diurnal cycle at Dome C reported in King *et al.* [2006]:  $H = 16 \pm 3 \text{ W m}^{-2}$  and  $G = 19 \pm 6 \text{ W m}^{-2}$  at 1200 LT and  $H = -7 \pm 1 \text{ W m}^{-2}$  and  $G = -18 \pm 5 \text{ W m}^{-2}$  at midnight LT. One can point out the larger thermodynamic contribution of the snow heat flux compared to the sensible heat flux in the surface energy budget during nighttime. At 2300 LT,  $H = -10.5 \text{ W m}^{-2}$  and  $G = -27.0 \text{ W m}^{-2}$ , while the net radiative cooling is equal to  $39 \text{ W m}^{-2}$  (not shown). The strong sensitivity of the surface temperature to snow thermal inertia as well as the large relative importance of the snow heat flux in the nocturnal surface energy budget echoes one of the conclusions from the GABLS3 experiment that states that the thermal coupling with the soil (snow) has the largest influence on the surface and near-surface temperatures in the stable ABL [Bosveld *et al.*, 2014]. This also highlights the need in GCMs to have a snow model that captures short time scales. Note that the above conclusions are weakly sensitive to the vertical resolution of the model as well as to the choice of the turbulent scheme in the ABL.

### 4.4. Setup of a Control Simulation for the Sensitivity Study to the Turbulent Mixing Formulations

In order to make a proper sensitivity analysis to the turbulent mixing parametrization in the next section, we set up a control simulation with more adapted surface parameters than in the STD-79 simulation and with a refined vertical resolution.

We consider the refined 90-level vertical grid jointly with the more appropriate values of the snow albedo and thermal inertia used in the new-snow-79 simulation. Note that we keep the default  $z_0 = 10^{-3} \text{ m}$  because it is close to the estimations for wind directions in the range met during the GABLS4 period [Vignon *et al.*, 2016].

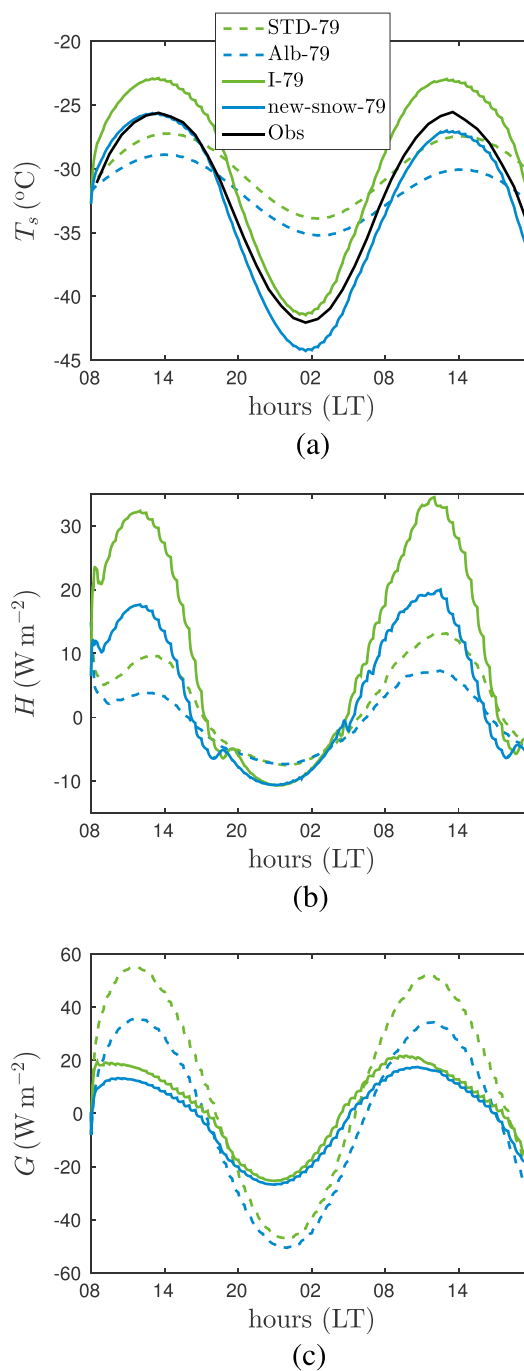


**Figure 5.** (a) Surface temperature, (b) surface sensible heat flux toward the air, and (c) conductive heat flux toward the snow for simulations with different snow albedo and snow thermal inertia.

However, as recommended in *Vignon et al.* [2016], we set the  $z_{0t}$  value to  $z_0/10 = 10^{-4}$  m. Following the conclusions of section 3.4, we use the K01  $f_m$  and  $f_h$  functions for the surface drag calculations.

The obtained control simulation (CTRL-90) shows more realistic structures of potential temperature and wind speed compared to the STD-79 simulation (Figures 4c and 4f). However, the near-surface vertical gradient of potential temperature during nighttime remains underestimated and the nocturnal jet remains too strong and too high. In addition to the sensitivity to the turbulent mixing formulations, the next section investigates the specific sensitivities of the ABL modelling to the change in vertical resolution, in the formulations of the drag stability functions and in  $z_{0t}$ .

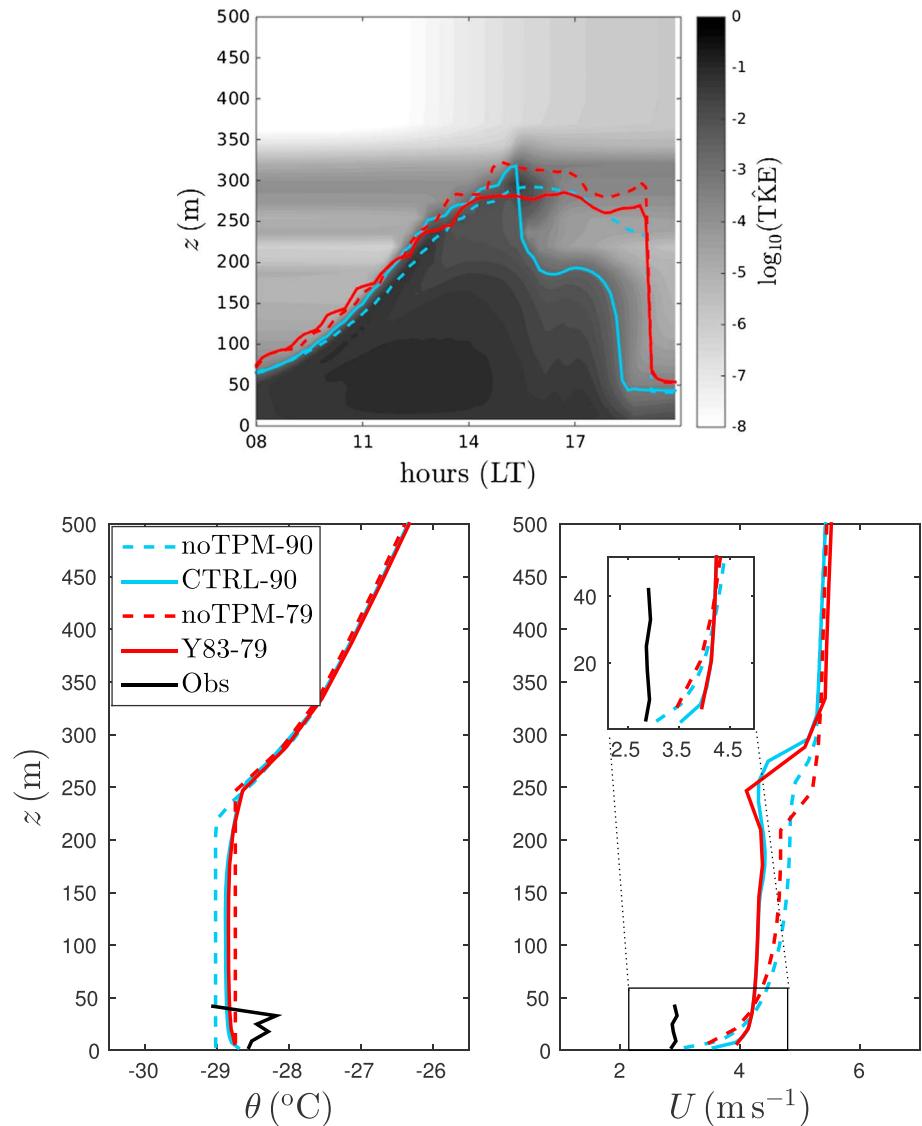


**Figure 6.** (top) Time series of  $h$  over the  $\log_{10}(\text{TKE})$  field in the CTRL-90 simulation during the second day of simulation. Vertical profiles of potential (bottom left) temperature and (bottom right) wind speed at 1400 LT in the second day of simulation. Simulations are carried out with two different vertical resolutions and with or without the thermal plume model. Due to convection at this time of the day, homogeneous profiles of  $\theta$  and  $U$  are expected. This is confirmed by observations within instrumental accuracy [Genthon et al., 2013].

## 5. Results of the Sensitivity Analysis to Turbulent Mixing Parametrizations

In this section, we present different sensitivity tests to turbulent mixing parametrizations with respect to the CTRL-90 simulation.

### 5.1. Diurnal Convective ABL: Sensitivity to the Use of the Thermal Plume Model

The representation of the convective ABL in LMDZ was shown to be improved by the use of the thermal plume model in tropical regions [e.g., Hourdin et al., 2015]. We explore here the effect of this scheme in modelling the weakly convective and dry diurnal ABL at Dome C. Figure 6 shows the time series of the ABL height during the second day of simulation and the vertical profiles of the potential temperature  $\theta$  and the wind speed at 1400 LT. Simulations with (resp. without) the thermal plume model are plotted in solid (resp. dashed) line for two vertical resolutions: the 79-level grid in red and the 90-level grid in blue. In Figure 6 (top), we show the turbulent layer in the CTRL-90 simulation (with the thermal plume model) by plotting in grey scale the quantity TKE defined as:

$$\text{TKE} = \text{TKE} + \hat{\alpha} \hat{w}^2 \tag{16}$$

The ABL height  $h$  is then diagnosed as the height at which TKE is equal to 5% of its values at the first model level. In Figure 6 (top), we see that this diagnostics gives an ABL height ranging between 45 and 320 m. These values fall in the range of daytime turbulent ABL heights estimated at Dome C in summer using 2011–2012 sodar observations, 40–340 m, in *Casasanta et al.* [2014]. However, comparing the different lines in Figure 6 (top), one can point out that the ABL height in the model is sensitive to the use of the thermal plume model and to the vertical resolution. For instance,  $h$  in the CTRL-90 simulation (solid blue line) drops earlier in the late afternoon compared to the other simulations.

One can further notice that the vertical profiles of both potential temperature (Figure 6, bottom left) and wind speed (Figure 6, bottom right) are less sensitive to the vertical resolution when the thermal plume model is activated. The use of the thermal plume model leads to weak wind speed gradients over the first 45 m in agreement with observations (black lines). Conversely, in simulations without the mass flux scheme, the vertical wind speed gradient over the first 50 m is significant. This confirms the ability of the thermal plume model to represent in a more physical way the vertical transport of momentum [*Hourdin et al.*, 2002, 2015]. However, the wind speed at 1400 LT over the first 45 m is overestimated by approximately  $1.2 \text{ m s}^{-1}$  in all the simulations. This can question the geostrophic wind forcing in the simulations. This point is further discussed for the nocturnal ABL in section 6.1.

## 5.2. Nocturnal ABL: Sensitivity to the Local Turbulent Diffusion Scheme

We now analyze the performances of the different local turbulent diffusion schemes in representing the very stable ABL during the GABLS4 night.

### 5.2.1. Vertical Structure of the Potential Temperature and Wind

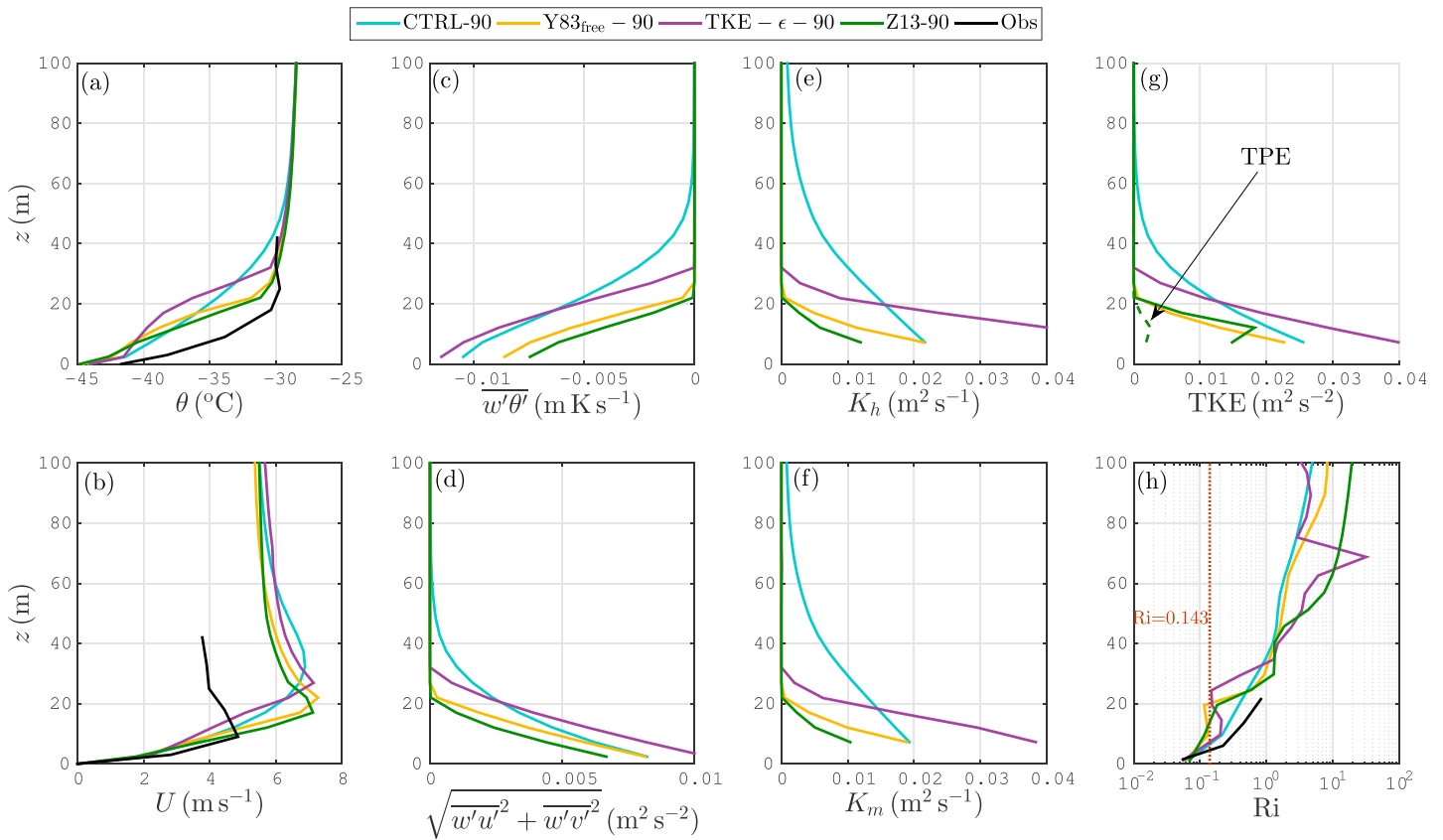
We compare four simulations that differ only by their local turbulence scheme: the default Y83 scheme, the Y83<sub>free</sub> scheme, the TKE- $\epsilon$  scheme, and the Z13 scheme (corresponding, respectively, to the CTRL-90, Y83<sub>free</sub>-90, TKE- $\epsilon$ -90, and Z13-90 simulations in Table 3).

Figure 7 shows vertical profiles of the potential temperature (a) and wind speed (b) in the first 100 m at 0100 LT, i.e., in the middle of the night. The vertical structures of the temperature and the wind speed during the whole experiment are depicted in Figure S1 in the supporting information. The potential temperature in the first 35 m is too cold in all the simulations compared to observations. The absence of large-scale subsidence in the forcings may explain a part of this bias (see section 6.3). Moreover, the vertical gradient of potential temperature in the first 10 m in the CTRL-90 and TKE- $\epsilon$ -90 simulations are significantly underestimated compared to the observed one ( $\approx 0.35 \text{ K m}^{-1}$ ) reflecting a significant excess of turbulent heat mixing. In particular, the vertical profile in the TKE- $\epsilon$ -90 simulation presents a marked concavity, i.e., an increase in the temperature inversion with an increase in height. In addition to better temperature profiles, one noticeable improvement in the Y83<sub>free</sub>-90 and Z13-90 simulations is a more distinct and lower nocturnal jet (green and yellow lines in Figure 7b). However, the nocturnal wind speed is overestimated in all the simulations, with values greater than  $6.5 \text{ m s}^{-1}$ , while the observed wind speed does not exceed  $5.5 \text{ m s}^{-1}$ .

Related to this systematic bias, Figure 8a shows that the wind veering over the first 42 m in the four simulations is underestimated compared to the observations. *van de Wiel et al.* [2010] underlines that the nocturnal inertial oscillation rotates around a virtual equilibrium wind vector that is close to the synoptic wind vector well above the jet peak. The amplitude of the nocturnal jet depends on the large-scale wind speed and also on the magnitude of the ageostrophic wind component at the time of momentum decoupling in the evening [see also *Baas et al.*, 2009]. The hodographs of the nocturnal wind at 42 m in Figure 8b show that the wind in the simulations and in the observations spins around a curvature center evidencing the inertial oscillation. The curvature center in the simulations is close to the geostrophic wind (red crosses) in agreement with the nocturnal jet theories. Nonetheless, the curvature center in simulations and observations looks different. It corresponds to a weaker and more southerly wind in the observations (dashed red arrow), suggesting an overestimated and too westerly geostrophic wind forcing in the simulations. The sensitivity to the geostrophic wind forcing is explored in section 6.

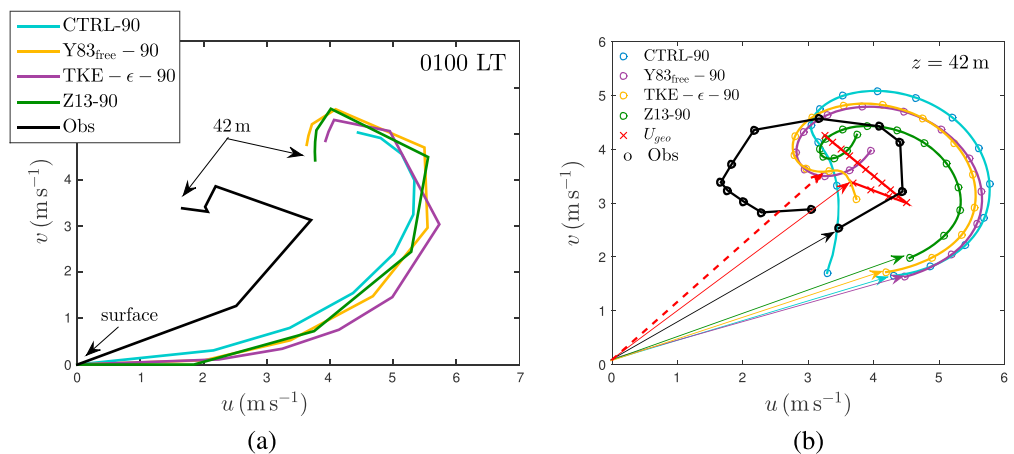
### 5.2.2. Vertical Structure of the Nocturnal Turbulence

Figure 7g shows the TKE vertical profiles at 0100 LT. Up to 20 m, the values of TKE are similar in all simulations but the Z13-90 that exhibits lower values. One can notice that the turbulent SBL at 0100 LT is much deeper in the CTRL-90 simulation compared to the others, with a significant level of TKE up to 60 m. For the Z13-90 simulation, the vertical profile of TPE is also plotted with a green dashed line. The TPE does not exceed 15% of TKE and plays a moderate role in the total turbulent energy during the GABLS4 night. Indeed, even though the ABL



**Figure 7.** Vertical profiles at 0100 LT over the first 100 m in four simulations that solely differ by their turbulence scheme. (a) Potential temperature, (b) wind speed, (c) turbulent heat flux, (d) magnitude of the turbulent momentum flux, (e) eddy diffusivity, (f) eddy viscosity, (g) TKE, and (h) Richardson number.

at 0100 LT is quite stable with Richardson number increasing from 0.05 to 1.5 in the first 40 m (Figure 7h), the contribution of the buoyancy to the TKE tendency is relatively small in all the simulations and the TKE budget is mainly driven by dissipation and wind shear production (see Appendix A). The buoyancy term being the exchange term between TKE and TPE [e.g., *Mauritsen et al., 2007*], obtaining a relatively small TPE compared to the TKE in the Z13-90 simulation, is thus consistent.



**Figure 8.** (a) ABL wind turning in the first 42 m at 0100 LT in observations and simulations. (b) Hodograph at 42 m between 1800 and 0700 LT in observations and simulations (each circle indicates an hourly mean datum). Red crosses show the geostrophic wind from the prescribed forcing for GABL54. Solid arrows indicate the wind at 1800 LT. The red dashed arrow indicates the constant geostrophic wind forcing used in experiments in section 6.1.

**Table 4.** Detailed Values of the Components of the Turbulent Exchange Coefficients at 0100 LT at Two Different Heights

Simulation	$\sqrt{\text{TKE}}$ ( $\text{m s}^{-1}$ )	$l_\epsilon$ (m)	$\mathcal{F}$	$Pr$	$K_m$ ( $\text{m}^2 \text{s}^{-1}$ )	$K_h$ ( $\text{m}^2 \text{s}^{-1}$ )
$z = 8 \text{ m}$						
CTRL-90	0.160	5.87	$2.06 \times 10^{-2}$	0.893	$1.93 \times 10^{-2}$	$2.16 \times 10^{-2}$
Y83 <sub>free</sub> -90	0.151	5.47	$2.30 \times 10^{-2}$	0.883	$1.89 \times 10^{-2}$	$2.14 \times 10^{-2}$
TKE- $\epsilon$ -90	0.195	5.67	$3.30 \times 10^{-2}$	0.714	$3.65 \times 10^{-2}$	$5.11 \times 10^{-2}$
Z13-90	0.124	1.74	$4.74 \times 10^{-2}$	0.870	$9.95 \times 10^{-3}$	$1.14 \times 10^{-2}$
$z = 18 \text{ m}$						
CTRL-90	0.146	5.87	$2.05 \times 10^{-2}$	0.893	$1.71 \times 10^{-2}$	$1.91 \times 10^{-2}$
Y83 <sub>free</sub> -90	0.074	1.97	$2.92 \times 10^{-2}$	0.864	$4.25 \times 10^{-3}$	$4.92 \times 10^{-3}$
TKE- $\epsilon$ -90	0.135	3.67	$3.30 \times 10^{-2}$	0.738	$1.63 \times 10^{-2}$	$2.20 \times 10^{-2}$
Z13-90	0.081	4.46	$6.02 \times 10^{-3}$	0.877	$2.19 \times 10^{-3}$	$2.49 \times 10^{-3}$

One can point out the significant differences between the vertical profiles of the turbulent heat flux (Figure 7c) and momentum flux (Figure 7d). Except CTRL-90 which has a nonzero heat flux up to 60 m, all the simulations show a heat flux whose magnitude decreases upward in the first 20 m. The vertical profile of the heat flux in the TKE- $\epsilon$ -90 is slightly concave. In fact, the divergence of the flux increases with height and it is responsible for the marked concavity of the potential temperature profile between 5 and 30 m.

To compare the  $K_m$  and  $K_h$  profiles in the different simulations (Figures 7e and 7f), we write them as

$$K_m = l_\epsilon \mathcal{F} \sqrt{\text{TKE}} \quad (17)$$

$$K_h = l_\epsilon \mathcal{F} Pr^{-1} \sqrt{\text{TKE}} \quad (18)$$

where  $l_\epsilon$  is the dissipation length scale (equation (5)) related to the size of the most energetic eddies [Hunt *et al.*, 1985; Cuxart *et al.*, 2006] and  $\mathcal{F}$  is a stability function. The detailed expressions of these terms in each scheme are given in section C, and their values at 0100 LT at two different heights in the stable turbulent layer are given in Table 4.

We observe that  $\sqrt{\text{TKE}}$ ,  $l_\epsilon$  and  $\mathcal{F}$  are generally greater at 8 m than at 18 m. Looking more into details, these three quantities continuously decrease with increasing height in all the simulations (not shown), except  $l_\epsilon$  in the Z13-90 simulation. This explains why  $K_h$  and  $K_m$  monotonically decrease with height (Figures 7e and 7f) and do not show a typical ‘‘cubic’’ profile as observed for the moderately stable GABLS1 case in Cuxart *et al.* [2006]. In the latter study,  $K_m$  and  $K_h$  in most models wax and wane with height, the increase being due to the increase in eddy size, and therefore  $l_\epsilon$ , with an increase in height. In the present GABLS4 simulations, the stratification is so strong that the turbulent diffusion decreases from the first model level.

We also notice that in the CTRL-90 simulation, at both 8 m and 18 m,  $l_\epsilon$  reaches a threshold value of 5.87 m imposed by the minimum of the mixing length  $l_{\min}$  (Table C1). Moreover, at 18 m,  $\mathcal{F}$  reaches a limit value of  $2.05 \times 10^{-2}$  imposed by the threshold value of the  $S_m$  function (Table C1). In fact, above a height of about 5 m, the Richardson number in the CTRL-90 simulation becomes greater than 0.143 (Figure 7h), i.e., the minimum value above which the  $S_m$  function is lower bounded (Figure 2). These two points raise the critical role of the thresholds of the mixing length and of the stability functions in the Y83 scheme. In the present simulations, such thresholds lead to an excess of mixing and deteriorate the representation of the nocturnal ABL.

Furthermore, it is worth noting in Table 4 that despite using the parametrization from Sukoriansky *et al.* [2005], the Prandtl number in the TKE- $\epsilon$ -90 simulation remains lower than 0.8. Even though the values of  $\sqrt{\text{TKE}}$  in the TKE- $\epsilon$ -90 and Y83<sub>free</sub>-90 are close to each other, the TKE- $\epsilon$  scheme also produces much larger values of  $l_\epsilon$  and  $\mathcal{F}$  and leads to larger  $K_m$  and  $K_h$ . The damping of turbulent diffusion by stability in the TKE- $\epsilon$  scheme is only accounted for in the reduction of the turbulent length scale. The departure of the vertical velocity scale from  $\sqrt{\text{TKE}}$  in stable conditions due to the anisotropy of turbulence is not considered, and in fact, using our notations, the stability function  $\mathcal{F}$  in the TKE- $\epsilon$  scheme is a constant equal to  $3.30 \times 10^{-2}$ .

In conclusion, despite the excess of large-scale wind speed that prevents a proper comparison with observations, the Y83<sub>free</sub>-90 and Z13-90 simulations have stronger vertical gradients of turbulence as well as sharper

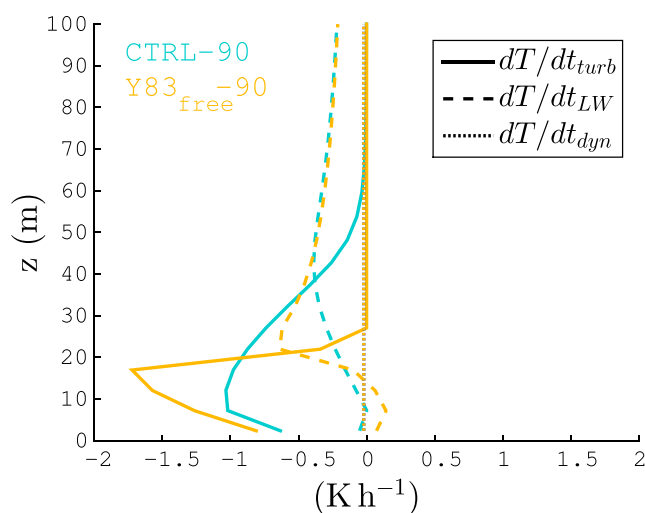


**Figure 9.** Vertical profiles of the temperature tendencies due to turbulence (solid lines), to longwave radiation (dashed lines), and to large-scale dynamical forcing (dotted lines) in the CTRL-90 (blue) and Y83<sub>free</sub>-90 (yellow) simulations at 0100 LT.  $dT/dt_{dyn}$  are small and superimposed.

and more realistic vertical gradients of wind and potential temperature compared to the default Y83 scheme and the TKE- $\epsilon$  scheme. As already mentioned in Ayotte *et al.* [1996], we have seen that setting lower bounds to  $S_m$  and  $S_h$  functions and the minimum mixing length has a nonnegligible effect on the GABLS4 simulations. To remove them seems to be a satisfactory first step to obtain a better representation of the summertime nocturnal ABL at Dome C in LMDZ at no additional numerical cost.

### 5.2.3. Temperature Tendencies in the ABL

Note that the weaker mixing in stable conditions gives more way to the longwave radiative divergence in the nocturnal ABL heat budget as shown by the decomposition of the temperature tendencies at 0100 LT in the Y83<sub>free</sub>-90 simulation compared to CTRL-90 (Figure 9). The dynamical tendency from the forcing ( $dT/dt_{dyn}$ ) is negligible in the ABL in both simulations. The turbulent cooling ( $dT/dt_{turb}$ ) is confined in the first 25 m in the Y83<sub>free</sub>-90 simulation, while it is significant up to 65 m in the CTRL-90 simulation. Above 15 m, the radiative cooling ( $dT/dt_{LW}$ ) is significant and it is larger (in magnitude) in the Y83<sub>free</sub>-90 simulation. In the latter simulation, the radiative cooling even dominates the air heat budget above 25 m and it reaches values down to  $-0.6 \text{ K h}^{-1}$ . Since almost no moisture condensation occurs in the nocturnal ABL in our simulations, the term  $dT/dt_{LW}$  is dominated by the clear-sky component (not shown). The critical role of the longwave radiative flux divergence in the energy budget of the near-surface nocturnal ABL is in agreement with the hypothesis in Vignon *et al.* [2016] stating that the heat exchange in stable conditions at Dome C may be partially driven or even dominated by radiation (see, e.g., Steeneveld *et al.* [2010] and Garratt and Brost [1981] for other regions). It is also worth noting that values of radiative cooling of  $-0.6 \text{ K h}^{-1} = -14.4 \text{ K d}^{-1}$  as observed in our simulations recall the observations of radiative cooling in the ABL at Summit, Greenland, in Hoch *et al.* [2007]. The simulated  $dT/dt_{LW}$  values are apparently consistent with atmospheric conditions over high and flat places over ice sheets.

### 5.2.4. Effects of the Vertical Resolution

After the partial conclusion that the use of the Y83<sub>free</sub> scheme leads to a reasonable structure of the nocturnal ABL in simulations with a refined 90-level vertical grid, we want to see to what extent this result is valid using the standard 79-level grid of LMDZ. In Figure 10, we show the temperature and wind speed structures in the first 100 m in simulations with the 90-level grid and with the 79-level grid using the Y83<sub>free</sub> scheme. The temperature field in the Y83<sub>free</sub>-79 simulation (Figure 10a) is very similar to that in the Y83<sub>free</sub>-90 (Figure 10b) and shows a little less mixing of heat near the surface during the night. The resolution change of the wind speed structure is small (Figures 10c and 10d). In particular, the nocturnal jet is well reproduced even using the 79-level grid. This augurs well for the representation of the summertime ABL over the Antarctic Plateau in 3-D simulations with the standard vertical grid of the model.

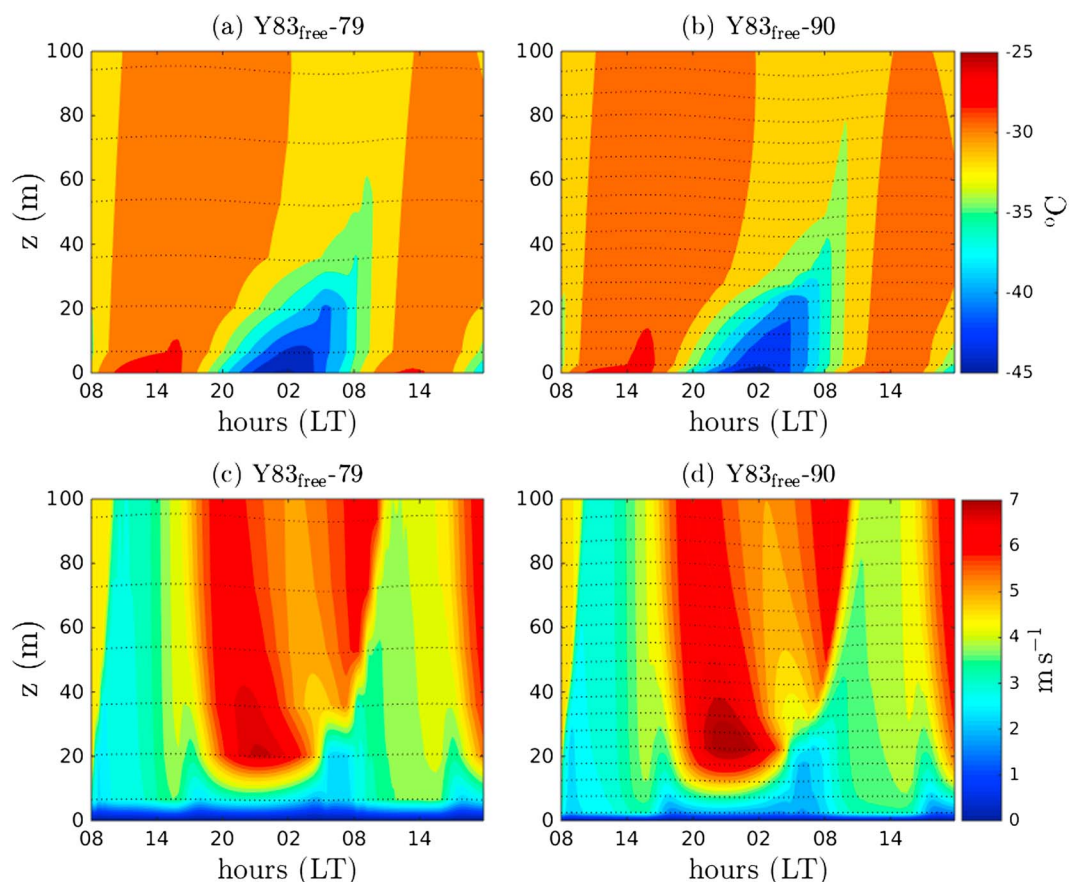


**Figure 10.** Vertical structures of the (a, b) temperature and (c, d) wind speed over the first 100 m above the ground in simulations with two different vertical resolutions,  $Y83_{free-79}$  and  $Y83_{free-90}$ . Dotted lines indicate the middle of model layers.

### 5.3. Surface Layer Scheme and Height of the First Model Level

We now explore the sensitivity to the surface layer scheme and to the height of the first model layer in simulations using the adapted  $Y83_{free}$  local turbulent scheme. A sensitivity test using the original value of  $z_{0t}, z_{0t} = z_0 = 10^{-3}$  m (instead of  $10^{-4}$  m), is also done in the simulation  $z_{0t}-90$ . Figures 11a and 11c show that with a first model level at 3 m, the flux calculation is not sensitive to the choice of the stability function in stable conditions (indicated by different colors) even in the middle of the night. Indeed, the bulk Richardson number between 3 m and the surface remains lower than 0.1 in all the simulations, i.e., in a range where the stability functions do not significantly differ (see Figure 3, in the  $Ri_b$  range to the left of the solid vertical line).

Both  $u_*$  and  $H$  compare relatively well with the direct estimations from temperature and wind observations at 3 m using the “bulk method” and stability functions from *King and Anderson* [1994] (see *Vignon et al.* [2016] for the details of the calculations). One can further notice that  $H$  is slightly overestimated (in magnitude) in all the simulations during nighttime. As expected, the magnitude of  $H$  is also larger in simulation  $z_{0t}-90$  because of the larger  $z_{0t}$  value. However, the absolute difference with the other simulations remains lower than  $1 \text{ W m}^{-2}$  during the whole experiment and the increase by 1 order of magnitude of  $z_{0t}$  appears not critical for the GABLS4 simulations. We now pay attention to simulations with the 89 vertical level grid, i.e., a grid similar to the 90-level grid except that the first model level height is 8 m instead of 3 m (simulations  $z1-L82-89$ ,  $z1-K01-89$ , and  $z1-MO-89$ ). Figures 11b and 11d show that the turbulent fluxes are similar to those calculated with the first model level at 3 m. During the night, fluxes are a bit more sensitive to the choice of the stability function since the bulk Richardson number computed between 8 m and the surface reach values up to 0.14. For  $Ri_b > 0.1$ , the fluxes calculated with the K01 and MO functions are smaller in amplitude than the fluxes calculated with the L82 functions used in LMDZ (see Figure 3, in the  $Ri_b$  range between the solid and dashed vertical brown lines). Differences reach  $0.01 \text{ m s}^{-1}$  for  $u_*$  and  $2 \text{ W m}^{-2}$  for  $H$ .

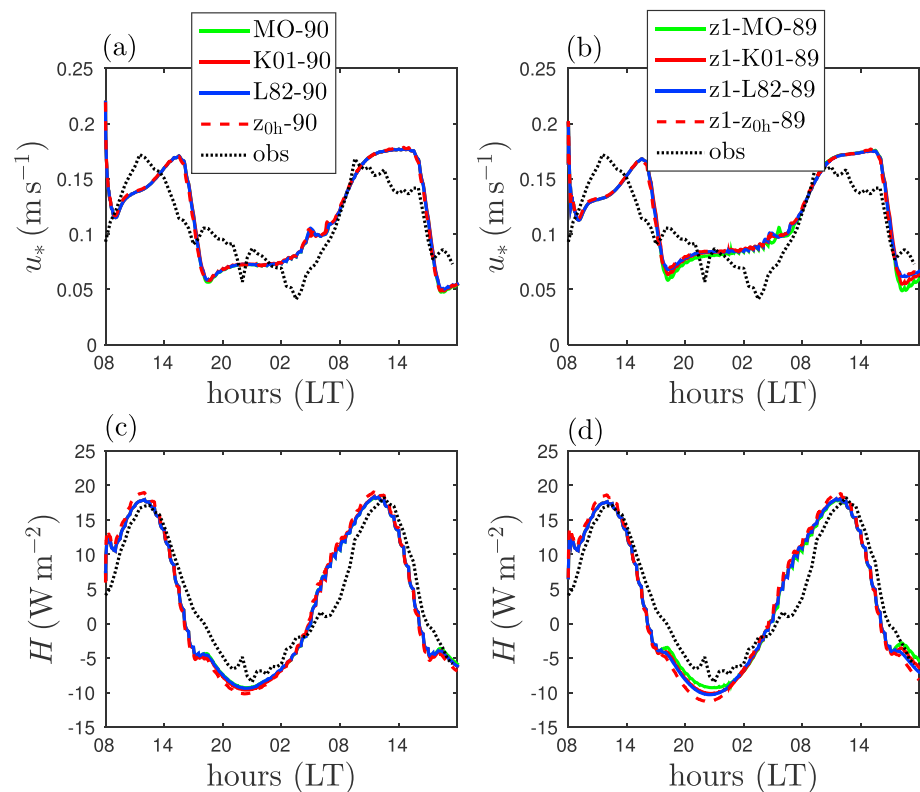


**Figure 11.** (a, b) Friction velocity and (c, d) surface sensible heat flux calculated with four couples of stability functions in stable conditions. Figures 11a and 11c (resp. Figures 11b and 11d) show simulations with a first model level at 3 m (resp. 8 m).

## 6. Experiments With Modified Forcings

### 6.1. Strength of the Geostrophic Wind Forcing

Baas *et al.* [2010] underlines the difficulty in SCM simulations to distinguish between differences due to parametrization schemes from the spread due to uncertainties in the forcings and particularly the forcing in wind. In our simulations, we particularly wonder what are the causes of the overestimated nocturnal wind speed near the surface. This bias could have various explanations like deficiencies in the physics used in the model and/or deficiencies in the forcings like the geostrophic wind. Indeed, a previous analysis of the nocturnal wind hodograph could suggest that the prescribed geostrophic wind speed is too strong. In this case, we can question to what extent our comparison with observations and our conclusions on the turbulence and surface layer schemes are correct. In order to assess the sensitivity to the geostrophic wind forcing, we have carried out simulations with a constant geostrophic wind forcing of  $4.75 \text{ m s}^{-1}$  that corresponds to the mean curvature center of the observed hodograph at 42 m (visually identified with a red dashed arrow in Figure 8b). In the middle of the night, this value is lower by about  $0.55 \text{ m s}^{-1}$  compared to the default forcing.

Figures 12c and 12d show the vertical profiles of potential temperature and wind speed at 0100 LT in simulations with this new geostrophic wind forcing. Even though the simulated temperature in the first 45 m remains too cold, both the simulated temperature and wind profiles are closer to observations than in the Reference simulations (Figures 12a and 12b; see also Figure S2 in the supporting information). In particular, the nocturnal jet shows a more realistic speed, but its height has not dramatically changed. However, the conclusions of the comparison between turbulence schemes and surface layer schemes that we draw in section 5.2 remain valid. We can, for instance, point out that the default Y83 scheme still gives an excessive mixing of heat and a too high and too deep nocturnal jet compared to the other turbulent schemes (see also the vertical profiles of turbulent quantities in Figure S3 in the supporting information).

### 6.2. Cold Nocturnal Bias at the Surface and Simulations With Prescribed Surface Temperature

A cold nighttime bias at the surface in the CTRL-90 simulation was pointed out in Figure 5a and remains present in all the other simulations presented so far. This bias cannot be attributed to the nocturnal turbulent

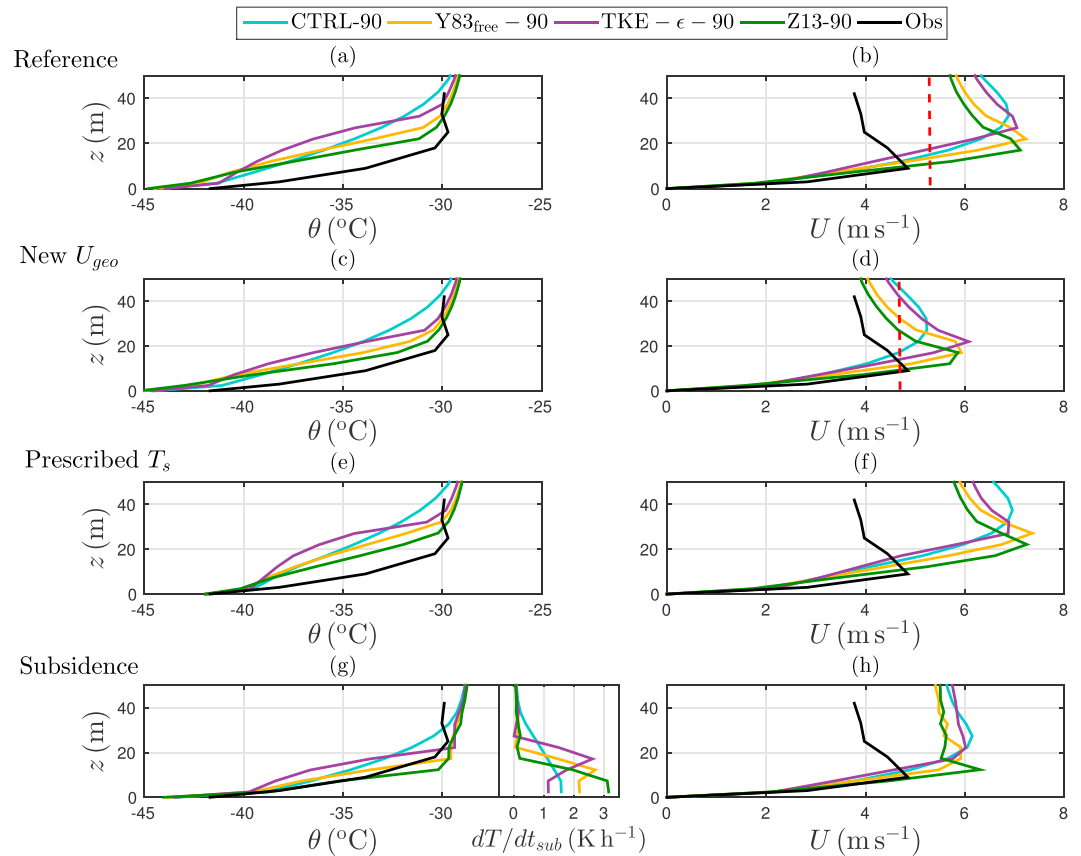


**Figure 12.** Vertical profiles of potential temperature and wind speed at 0100 LT in simulations with different forcings. (a, b) "Reference" refers to simulations with classical forcings, (c, d) "new Ugeo" refers to simulation with the constant geostrophic wind forcing identified by a red dashed arrow in Figure 8b, (e, f) "prescribed Ts" refers to simulations with prescribed surface temperature, and (g, h) "subsidence" refers to the simulations with a prescribed large-scale subsidence. In Figures 12b and 12d, the value of the speed of the geostrophic wind forcing is indicated with a red dashed line. In the inset in Figure 12g is the plotted temperature tendency associated to the subsidence.

heat flux because its amplitude is more likely overestimated rather than underestimated due to an excess in the near-surface wind or in the turbulent mixing. Figure 13 shows that our simulations underestimate the

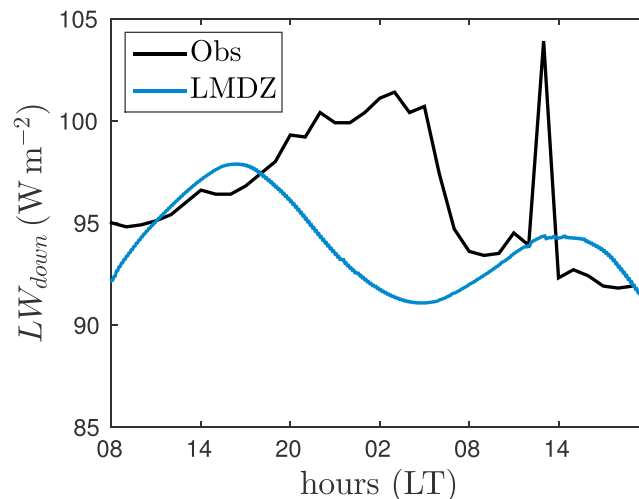


**Figure 13.** Time series of the  $LW_{down}$  in the  $Y83_{free-90}$  simulation (blue lines) and in observations (black line).

downward radiative flux at the surface ( $LW_{down}$ ) during the night. This can be critical since  $LW_{down}$  is the major heat supply at the surface, and the amplitude of the deficit in  $LW_{down}$  could explain a significant part of the cold bias at the surface. The source of this deficit in  $LW_{down}$  can be hardly attributed to a bad representation of the water vapor vertical profile since the lateral forcing of the single column model is quite consistent with radiosoundings. A likely deficiency of the longwave radiative transfer in such conditions in LMDZ would agree with Wild *et al.* [2001]. The authors evidenced large negative biases of  $LW_{down}$  in cold and dry conditions over the South Pole in the ECMWF ERA-15 reanalyses that were produced using the same radiative code as

LMDZ for the longwave spectrum, i.e., the scheme developed in *Morcrette et al.* [1986]. These biases were significantly reduced when the Rapid Radiative Transfer Model was implemented during the development of the ERA-40 reanalyses [*Morcrette et al.*, 2001].

Furthermore, although the magnitude of the observed longwave radiation does not correspond to a significant transit of clouds above the Antarctic Plateau [e.g., *Town et al.*, 2005], the lack of nighttime  $LW_{\text{down}}$  might also be a consequence of an underestimation of the hydrometeors concentration in the atmosphere. In fact, the model simulates a small amount of condensed water into ice particles (up to  $3 \times 10^{-6} \text{ kg kg}^{-1}$ ) between 2500 and 3000 m above ground level leading to a difference between the  $LW_{\text{down}}$  at the surface and its clear-sky component of  $1.5 \text{ W m}^{-2}$  in the middle of the night. However, this process could be underrepresented or not well simulated due to a too coarse vertical resolution in the middle troposphere or to failures in the microphysics scheme. To assess the performances of the radiative and microphysics schemes in LMDZ over Antarctica is beyond the scope of the present paper, but this requires a further thorough study.

One can wonder if our conclusions on the sensitivity to the turbulent scheme and to the surface layer schemes are still valid with a correct  $LW_{\text{down}}$  at the surface and a surface temperature closer to observations. We have thus carried out simulations in which we force the surface temperature with observations, like in the second stage of the GABLS4 experiment [*Bazile et al.*, 2015].

Vertical profiles of potential temperature and wind speed in the aforesaid simulations are plotted in Figures 12e and 12f. No major difference can be identified compared to the "Reference" simulation, i.e., with a free  $T_s$  (Figures 12a and 12b), except of course for the surface temperature itself. We remark that the cold bias in the first 45 m is still present in all the simulations, and it is of similar amplitude compared to the control simulations. The near-surface atmospheric cold bias in the simulation is thus probably not only driven by the surface cold bias but a consequence of an excess of turbulent cooling in the stable ABL and/or to the lack of a large-scale subsidence forcing.

### 6.3. Large-Scale Subsidence

Subsidence has been shown to affect the structure of the stable ABL, bringing down warmer air from aloft [*Carlson and Stull*, 1986; *Mirocha and Kosović*, 2010]. The atmosphere above the Antarctic Plateau experiences a large-scale subsidence due to the divergence of the continental scale surface drainage flow [*James*, 1989]. Comparing sodar measurements of the ABL height to estimations with an analytical model, *Argentini et al.* [2005], *King et al.* [2006], and *Pietroni et al.* [2012] expect the subsidence velocities to reach up to a few centimeters per second at the top of the daytime Dome C ABL in summer. Assuming that the horizontal divergence is constant with height, the subsidence could be estimated from a network of in situ wind measurements. However, such a network has not been set up around Dome C and to the authors' knowledge, the exact subsidence velocity at Dome C remains unknown. Here we attempt to assess the effect of a large-scale subsidence typical rate on the nocturnal temperature and wind profiles. We thus make idealized experiments in which we add an additional vertical subsidence of  $10^{-3} \text{ m s}^{-1}$  in the reference forcings. This value has been chosen because it is close to the December mean value in the first 100 m above Dome C that is found in a 10 year climatological simulation with the full 3-D LMDZ model:  $1.2 \times 10^{-3} \text{ m s}^{-1}$ . Results are shown in Figures 12g and 12h. The simulated temperature profiles are closer to observations compared to the reference simulations, with stronger vertical gradients near the surface in agreement with *Mirocha and Kosović* [2010]. In particular, the cold bias in the first 25 m is significantly reduced in response to the warming rates associated to the subsidence (inset in Figure 12g). These latter reach a few  $\text{K h}^{-1}$  in the first 25 m where the vertical gradient of the potential temperature is strong. These values are of the same order of magnitude than the turbulent cooling rates. The surface temperature is also higher by approximately  $1^\circ\text{C}$  compared to the reference simulations. In addition to the underestimated downward longwave fluxes, the subsidence is thus a good candidate to explain the cold nocturnal bias at the surface in our simulations. However, one can also point out that the structure of the nocturnal jet is degraded (Figure 12h) compared to the Reference simulations. This aspect can be improved using a more adapted geostrophic wind forcing as in section 6.1, leading to a weaker but sharper nocturnal jet (not shown).

## 7. Conclusions

The single column version of the LMDZ GCM has been evaluated in the framework of the GABLS4 exercise. This experiment consists in modelling a typical and climatological summer diurnal cycle at Dome C on the East

Antarctic Plateau. A sensitivity study to surface parameters, vertical grid, turbulent mixing parametrization, and forcings has been carried out and have led to the following conclusions:

1. The default snow albedo value in the model (0.77) was too small for typical Dome C summer conditions and led to excessive diurnal surface temperature and sensible heat flux. Using a realistic albedo of 0.81 leads to more realistic diurnal temperatures. Moreover, the default snow thermal inertia over ice sheets of  $2000 \text{ J m}^{-2} \text{ K}^{-1} \text{ s}^{-1/2}$  was very overestimated. Using a more realistic value for the surface snow at Dome C leads to a much better amplitude of the diurnal cycle of temperature.
2. Including the thermal plume model does not significantly change the mixing of heat in the dry and weakly convective conditions during daytime, but it improves the mixing of momentum in the first meters of the ABL.
3. Two additional turbulent diffusion schemes have been tested and compared to the original 1.5 order closure Y83 scheme. While the Y83 and the TKE- $\epsilon$  schemes lead to an excessive mixing of heat and momentum in the first tens of meters during the night, the Y83<sub>free</sub> and Z13 schemes produce realistic strong vertical gradients of potential temperature and wind speed. In fact, best simulations are those in which the turbulence cuts off above 35 m in the middle of the night, giving more way to the longwave radiative flux divergence in the nocturnal ABL heat budget. Removing the thresholds of stability functions and the minimum mixing length in the Y83 scheme seems to be a good trade-off to obtain more realistic sharp vertical gradients in the stable ABL without changing completely the current turbulence code and adding numerical cost. This conclusion is valid for both the refined 90 levels resolution and the 79 levels standard resolution. Hence, with the standard vertical resolution of the model, we would recommend the configuration of the Y83<sub>free</sub>-79 simulation for modelling the summer Antarctic ABL in LMDZ. Removing thresholds in the turbulence schemes to correctly model the stable ABL over the Antarctic Plateau also raises the need to parametrize more explicitly the additional sources of sub-grid mixing in other regions of the globe, like the gravity wave-induced terrain drag [Steenefeld *et al.*, 2008] for instance.
4. Short tail stability functions of the surface drag coefficient compare better with in situ observations in stable conditions at Dome C. In particular, the L82 functions in the standard version of LMDZ are strongly overestimated. However, the dependence to the choice of the stability functions in stable conditions is not critical for the GABLS4 case, since the near-surface stability during the night is not strong enough to distinguish between functions. It is especially true if the first model level layer is at 3 m rather than 8 m. Further sensitivity tests to the surface layer scheme under weaker wind conditions or in winter are therefore required.
5. The geostrophic wind forcing of the single column model also seems overestimated during nighttime. Simulations with a weaker wind forcing corresponding to the curvature center of the observed inertial oscillation at the top of the 45 m tower show better wind speed profiles. However, this does not change the main conclusions on the comparison between turbulence and surface drag schemes.
6. We observe an underestimation of downward longwave flux at the surface in all the simulations that is expected to be partly responsible for the cold bias at the surface during nighttime. This probably reflects a failure of the cloud cover modelling or a deficiency of the current radiative scheme in the dry and cold Antarctic air. Imposing surface temperature does not prevent, however, from a near-surface cold bias in the nighttime ABL.
7. This cold bias points to the possible lack of subsidence in the GABLS4 forcing. Adding such a forcing with a typical vertical velocity retrieved from climate simulations would reconcile model and observations both in terms of ABL temperature and of height of the nocturnal jet.

Although the present work focuses on one particular GCM, the types of parametrization (ABL turbulence, surface fluxes, and heat diffusion in the snow) that we have evaluated are common in climate and weather forecast models. Our results of sensitivity tests and the aforelisted conclusions can thus be extended and to some extent interpreted as recommendations to the climate modelling community to obtain a reasonable representation of the clear-sky summertime ABL over the Antarctic Plateau. In particular, (i) it is critical to ascertain whether the snow scheme can capture fast time scales, (ii) it is important to check whether the turbulent diffusion scheme does not maintain artificial mixing and enables a cutoff of turbulence at a few meters above the surface, (iii) typical vertical resolutions with three vertical levels in the first 50 m above the surface seems sufficient for state-of-the-art GCMs to capture the overall dynamics of the summertime Dome C ABL; nonetheless, such a conclusion should be taken with a pinch of salt and not hastily generalized to the wintertime very stable ABLs.

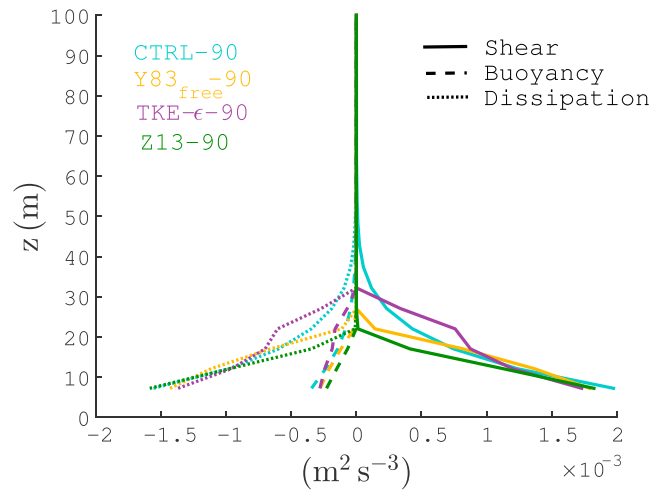


**Figure A1.** Vertical profiles of the three main contributions to the TKE tendency at 0100 LT in four simulations.

Finally, our study has enabled a first evaluation of the performances of LMDZ over the Antarctic Plateau and it is a good starting point for carrying out three-dimensional simulations, particularly during the polar night when the ABL can be very stable. It will be particularly interesting to test whether our current generation GCM is not only capable of simulating specific cases like the present one but also if it can capture general system responses of the stable ABL, such as sudden regime transitions between weakly and very stable regimes, as extensively discussed in Vignon *et al.* [2017], van de Wiel *et al.* [2017], and Walters *et al.* [2007]. Moreover, accurate modelling of very stable ABL over the Antarctic Plateau requires a correct modelling of the longwave radiative

transfer that rests on a good representation of the atmospheric water content in the ABL. This may challenge the current microphysics parametrizations in climate models, since strong near-surface supersaturations with respect to ice occur frequently at Dome C, particularly during the polar night [Genthon *et al.*, 2017].

### Appendix A: TKE Prognostic Equation and TKE Budget at 0100 LT

The TKE prognostic equation that is solved in the LMDZ model whatever the turbulence scheme is

$$\frac{\partial \text{TKE}}{\partial t} = \underbrace{\frac{\partial}{\partial z} \left( \rho K_e \frac{\partial \text{TKE}}{\partial z} \right)}_{\text{Turbulent diffusion}} - \underbrace{u'w' \frac{\partial u}{\partial z} - v'w' \frac{\partial v}{\partial z}}_{\text{Shear}} + \underbrace{\frac{g}{\theta_v} w' \theta_v'}_{\text{Buoyancy}} - \underbrace{\epsilon}_{\text{Dissipation}} \quad (\text{A1})$$

with  $u$  and  $v$  the zonal and meridional components of the wind,  $\theta_v$  the virtual potential temperature,  $\rho$  the air density,  $u'w'$  and  $v'w'$  the components of the turbulent momentum flux,  $\frac{g}{\theta_v} w' \theta_v'$  the buoyancy flux, and  $K_e$  a turbulent diffusion coefficient. Figure A1 shows the vertical profiles at 0100 LT of the three main contributions to the TKE tendency. One can notice that for all the turbulent schemes, the TKE budget is primarily driven by the “Shear” and “Dissipation” terms.

### Appendix B: First-Order-Like Stability Functions of the 1.5 Order Closure Y83 Scheme

Assuming steady state for the TKE equation (equation (A1)), the formulations of turbulent diffusion coefficients can read like an expression equivalent to the mixing coefficient from first-order schemes [Cuxart *et al.*, 2006]. In the surface layer where  $l \approx \kappa z$ , the turbulent exchange coefficients read [Mellor and Yamada, 1982]

$$K_m = (\kappa z)^2 \underbrace{(B_1 S_m^3 (1 - Ri/Pr))^{1/2}}_{F_m} \frac{\partial U}{\partial z} \quad (\text{B1a})$$

$$K_h = (\kappa z)^2 \underbrace{(B_1 (1 - Ri/Pr))^{1/2} S_m^{3/4} S_h}_{F_h} \frac{\partial U}{\partial z} \quad (\text{B1b})$$

where  $F_m$  and  $F_h$  are “first-order”-like stability functions and  $Pr = K_m/K_h = S_m/S_h$  is the turbulent Prandtl number.  $F_m$  and  $F_h$  functions are equivalent to the  $f_m$  and  $f_h$  functions used to calculate the surface drag coefficients [England and McNider, 1995].

**Table C1.** Expressions of  $l_e$ ,  $\mathcal{F}$  and  $Pr$  in Each Turbulent Scheme

Scheme	$l_e$	$\mathcal{F}$	$Pr$
Y83	$\max(B_1 l_2^{-3/2}, 5.87)$	$\max(4/B_1 S_m, 2.05 \times 10^{-2})$	$\min\left(1.318 \frac{0.2231 - R_{if}}{0.2341 - R_{if}}, 0.893\right)$
Y83 <sub>free</sub>	$B_1 l_2^{-3/2}$	$4/B_1 S_m$	$1.318 \frac{0.2231 - R_{if}}{0.2341 - R_{if}}$
TKE- $\epsilon$	$\frac{TKE^{3/2}}{\epsilon}$	$c_\mu$	Sukoriansky et al. [2005]
Z13	$\sqrt{TKE} t_\epsilon$	$2C_r A_z$	$\frac{C_r}{C_f} \left(1 - \frac{C_\theta TPE}{A_z TKE}\right)^{-1}$

## Appendix C: $K_m$ and $K_h$ Decomposition

In all the turbulent schemes used in LMDZ,  $K_m$  and  $K_h$  coefficients can be written using equation (17). The expression of the terms  $l_e$ ,  $\mathcal{F}$  and  $Pr$  in each scheme with the appropriate variables and parameters is detailed in Table C1.

### Acknowledgments

We are grateful to Fleur Couvreur, H elene Barral, Gerhard Krinner, Fr ed eric Cheruy, and Peter Baas for fruitful discussions. This work was supported by the French National Program LEFE, INSU (programs CLAPA, DEPHY, and GABLS4), and OSUG (GLACIOCLIM observatory). Logistical support for field observations by the French (IPEV) and Italian (PNRA) polar agencies through "programme CALVA" (1013) and the "CoMPASS project" is gratefully acknowledged. Meteorological data obtained in the framework of CALVA are made available on the website <http://lgge.osug.fr/~genthon/calva/home.shtml> or on request to the authors. We thank the WRCP-BSRN network and Christian Lanconelli for dissemination of the radiation data and Stefania Argentini and Giampietro Casasanta for providing sonic anemometer data. We also thank three anonymous reviewers for their careful evaluation of the manuscript and thoughtful comments.

### References

- Agosta, C., V. Favier, G. Krinner, H. Gall e, and C. Genthon (2013), High resolution modelling of the Antarctic surface mass balance, application for the twentieth, twenty first and twenty second centuries, *Clim. Dyn.*, *41*, 3247–3260, doi:10.1007/s00382-013-1903-9.
- Ait-Mesbah, S., J.-L. Dufresne, F. Cheruy, and F. Hourdin (2015), The role of thermal inertia in the representation of mean and diurnal range of surface temperature in semiarid and arid regions, *Geophys. Res. Lett.*, *42*, 7252–7580, doi:10.1002/2015GL065553.
- Anderson, P. S. (2009), Measurement of Prandtl number as a function of richardson number avoiding self-correlation, *Boundary Layer Meteorol.*, *131*, 345–362.
- Andreas, E. L. (1987), A theory for the scalar roughness and the scalar transfer coefficients over snow and sea ice, *Boundary Layer Meteorol.*, *38*, 159–184.
- Argentini, S., A. Viola, A. M. Sempreviva, and I. Petenko (2005), Summer boundary-layer height at the plateau site of Dome C, Antarctica, *Boundary Layer Meteorol.*, *115*, 409–422, doi:10.1007/s10546-004-5643-6.
- Argentini, S., I. Pietroni, G. Mastrantonio, A. P. Viola, G. Dargaud, and I. Petenko (2014), Observations of near surface wind speed, temperature and radiative budget at Dome C, Antarctic Plateau during 2005, *Antarct. Sci.*, *26*, 104–112, doi:10.1017/S0954102013000382.
- Ayotte, K. W., et al. (1996), An evaluation of neutral and convective boundary-layer parametrizations relative to large eddy simulations, *Boundary Layer Meteorol.*, *79*, 131–175.
- Baas, P., F. C. Bosveld, H. K. Baltink, and A. A. M. Holtslag (2009), A climatology of nocturnal low-level jets at Cabauw, *J. Appl. Meteorol. Climatol.*, *48*(8), 1627–1642, doi:10.1175/2009JAMC1965.1.
- Baas, P., F. C. Bosveld, G. Lenderik, E. van Meijgaard, and A. A. M. Holtslag (2010), How to design single-column model experiments for comparison with observed nocturnal low-level jets, *Q. J. R. Meteorol. Soc.*, *48*(136), 671–684, doi:10.1002/qj.592.
- Barral, H., E. Vignon, E. Bazile, O. Traull e, H. Gall e, C. Genthon, C. Brun, F. Couvreur, and P. Le Moigne (2014), Summer diurnal cycle at Dome C on the Antarctic Plateau, 21st Symposium on Boundary Layer and Turbulence, Jun 2014, Leeds, U. K.
- Bazile, E., F. Couvreur, P. Le Moigne, C. Genthon, A. A. M. Holtslag, and G. Svensson (2014), GABLS4: An intercomparison case to study the stable boundary layer over the Antarctic plateau, *Global Ener. Water Cycle Exper. News*, *24*(4).
- Bazile, E., F. Couvreur, P. Le Moigne, and C. Genthon (2015), First workshop on the GABLS4 experiment, *Global Ener. Water Cycle Exper. News*, *25*(3).
- Blackadar, A. K. (1962), The vertical distribution of wind and turbulent exchange in neutral atmosphere, *J. Geophys. Res.*, *67*, 3095–3102.
- Bosveld, F. C., et al. (2014), The third gabls intercomparison case for evaluation studies of boundary-layer models. Part B: Results and process understanding, *Boundary Layer Meteorol.*, *152*(2), 157–187, doi:10.1007/s10546-014-9919-1.
- Brun, E., et al. (2012), Snow/atmosphere coupled simulation at Dome C, Antarctica, *J. Glaciol.*, *52*(204), 721–736.
- Carlson, M. A., and R. B. Stull (1986), Subsidence in the nocturnal boundary layer, *J. Clim. Appl. Meteorol.*, *25*(8), 1088–1099, doi:10.1175/1520-0450(1986)025<1088:SITNBL>2.0.CO;2.
- Casasanta, G., I. Pietroni, I. Petenko, and S. Argentini (2014), Observed and modelled convective mixing-layer height at Dome C, Antarctica, *Boundary Layer Meteorol.*, *151*, 587–608, doi:10.1007/s10546-014-9907-5.
- Cassano, J. J., T. R. Parish, and J. C. King (2001), Evaluation of turbulent surface flux parameterizations for the stable surface layer over Halley, Antarctica, *Mon. Weather Rev.*, *129*, 26–46.
- Conolley, W. M. (1996), The Antarctic temperature inversion, *Int. J. Climatol.*, *16*, 1333–1342.
- Cosme, E., F. Hourdin, C. Genthon, and P. Martinerie (2005), Origin of dimethylsulfide, non-sea-salt sulfate, and methanesulfonic acid in eastern Antarctica, *J. Geophys. Res.*, *110*, D03302, doi:10.1029/2004JD004881.
- Cuxart, J., et al. (2006), Single-column model intercomparison for a stably stratified atmospheric boundary layer, *Boundary Layer Meteorol.*, *118*(2), 273–303, doi:10.1007/s10546-005-3780-1.
- Deardorff, J. W. (1980), Stratocumulus-capped mixed layers derived from a three dimensional model, *Boundary Layer Meteorol.*, *18*, 495–527.
- Delage, Y. (1997), Parametrising sub-grid scale vertical transport in atmospheric models under statically stable conditions, *Boundary Layer Meteorol.*, *82*, 23–48.
- Deleersnijder, E. (1992), Mod elisation hydrodynamique tridimensionnelle de la circulation g en erale estivale de la r egion du d etroit de bering (in French), PhD thesis, Universit e Catholique de Louvain, Belgium.
- Derbyshire, S. H. (1999), Boundary-layer decoupling over cold surfaces as a physical boundary-instability, *Boundary Layer Meteorol.*, *90*, 297–325.
- Dufresne, J.-L., et al. (2013), Climate change projections using the IPSL-CM<sub>5</sub> earth system model: From CMIP3 to CMIP5, *Clim. Dyn.*, *40*(9), 2123–2165, doi:10.1007/s00382-012-1636-1.

- Dutra, E., I. Sandu, G. Balsamo, A. Beljaars, H. Freville, E. Vignon, and E. Brun (2015), *Understanding the ECMWF Winter Surface Temperature Biases Over Antarctica*, vol. 762, European Center for Medium Range Weather Forecast Technical Memorandum.
- Duynkerke, P. G. (1988), Application of the E-epsilon turbulence closure model to the neutral and stable atmospheric boundary layer, *J. Atmos. Sci.*, *45*, 865–880.
- England, D. E., and R. T. McNider (1995), Stability functions based upon shear functions, *Boundary Layer Meteorol.*, *74*, 113–130.
- Esau, I., and A. A. Grachev (2007), Turbulent Prandtl number in stably stratified atmospheric boundary layer: Intercomparison between LES and SHEBA data, *e-WindEng*, *5*, 1–17.
- Gallée, H., and I. Gorodetskaya (2010), Validation of a limited area model over Dome C, Antarctic Plateau, during winter, *Clim. Dyn.*, *23*, 61–72, doi:10.1007/s00382-008-0499-y.
- Gallée, H., and G. Schayes (1994), Development of a three-dimensional meso-gamma primitive equation model, katabatic winds simulation in the area of Terra Nova Bay, Antarctica, *Mon. Weather Rev.*, *12*, 671–685.
- Gallée, H., H. Barral, E. Vignon, and C. Genthon (2015a), A case study of a low level jet during OPALE, *Atmos. Chem. Phys.*, *15*, 1–18, doi:10.5194/acp-15-1-2015.
- Gallée, H., et al. (2015b), Characterization of the boundary layer at Dome C (East Antarctica) during the OPALE summer campaign, *Atmos. Chem. Phys.*, *15*, 6225–6236, doi:10.5194/acp-15-6225-2015.
- Garratt, J. R., and R. A. Brost (1981), Radiative cooling effects within and above the nocturnal boundary layer, *J. Atmos. Sci.*, *38*, 2370–2745.
- Genthon, C., G. Krinner, and E. Cosme (2002), Free and laterally nudged Antarctic climate of an atmospheric general circulation model, *Mon. Weather Rev.*, *130*, 1601–1616.
- Genthon, C., M. S. Town, D. Six, V. Favier, S. Argentini, and A. Pellegrini (2010), Meteorological atmospheric boundary layer measurements and ECMWF analyses during summer at Dome C, Antarctica, *J. Geophys. Res.*, *115*, D05104, doi:10.1029/2009JD012741.
- Genthon, C., D. Six, H. Gallée, P. Grigioni, and A. Pellegrini (2013), Two years of atmospheric boundary layer observations on a 45-m tower at Dome C on the Antarctic plateau, *J. Geophys. Res. Atmos.*, *118*, 3218–3232, doi:10.1002/jgrd.50128.
- Genthon, C., D. Six, C. Scarchilli, V. Ciardini, and M. Frezzotti (2015), Meteorological and snow accumulation gradients across Dome C, East Antarctic plateau, *Int. J. Climatol.*, *36*, 455–466, doi:10.1002/joc.4362.
- Genthon, C., L. Piard, E. Vignon, J.-B. Madeleine, M. Casado, and H. Gallée (2017), Atmospheric moisture supersaturation in the near-surface atmosphere at Dome C, Antarctic Plateau, *Atmos. Chem. Phys.*, *17*, 1–14, doi:10.5194/acp-17-1-2017.
- Grenfell, T. C., and S. G. Warren (1994), Reflection of solar radiation by the Antarctic snow surface at ultraviolet, visible, and near-infrared wavelengths, *J. Geophys. Res.*, *99*(D9), 18,669–18,684.
- Hoch, S. W., P. Calanca, R. Philipona, and A. Ohmura (2007), Year-round observation of longwave radiative flux divergence in Greenland, *J. Appl. Meteorol.*, *46*, 1469–1479, doi:10.1175/JAM2542.1.
- Holtzlag, A. A. M. (2006), GEWEX Atmospheric Boundary-Layer Study (GABLS) on stable boundary layers, *Boundary Layer Meteorol.*, *118*, 243–246, doi:10.1007/s10546-005-9008-6.
- Holtzlag, A. A. M., G. Svensson, S. Basu, B. Beare, F. C. Bosveld, and J. Cuxart (2011), Overview of the GEWEX Atmospheric Boundary Layer Study (GABLS), paper presented at the Workshop on Diurnal Cycles and the Stable Boundary Layer, Shinfield Park, Reading, U. K., 7–10 Nov.
- Holtzlag, A. A. M., et al. (2013), Stable boundary layers and diurnal cycles, *Bull. Am. Meteorol. Soc.*, *94*, 1691–1706, doi:10.1175/BAMS-D-11-00187.1.
- Hourdin, F. (1992), Etude et simulation numérique de la circulation générale des atmosphères planétaires (in French), PhD thesis, Laboratoire de Météorologie Dynamique, Paris.
- Hourdin, F., F. Couvreux, and L. Menut (2002), Parameterization of the dry convective boundary layer based on a mass flux representation of thermals, *J. Atmos. Sci.*, *59*, 1105–1123.
- Hourdin, F., et al. (2013), Lmdz5b: The atmospheric component of the ipsl climate model with revisited parameterizations for clouds and convection, *Clim. Dyn.*, *40*(9), 2193–2222, doi:10.1007/s00382-012-1343-y.
- Hourdin, F., M. Gueye, B. Diallo, J.-L. Dufresne, J. Escribano, L. Menut, B. Marticoréna, G. Siour, and F. Guichard (2015), Parameterization of convective transport in the boundary layer and its impact on the representation of the diurnal cycle of wind and dust emissions, *Atmos. Chem. Phys.*, *15*, 6778–6788, doi:10.5194/acp-15-6775-2015.
- Hudson, S., and R. E. Brandt (2005), A look at the surface based temperature inversion on the Antarctic plateau, *J. Clim.*, *118*, 1673–1696.
- Hunt, J. C. R., J. C. Kaimal, and J. E. Gaynor (1985), Some observations of turbulence structure in stable layers, *Q. J. R. Meteorol. Soc.*, *111*, 793–815.
- James, I. M. (1989), The Antarctic drainage flow: Implications for hemispheric flow on the Southern Hemisphere, *Antarct. Sci.*, *1*, 279–290.
- King, J. C. (1990), Some measurements of turbulence over an Antarctic ice-shelf, *Q. J. R. Meteorol. Soc.*, *116*, 379–400.
- King, J. C., and P. S. Anderson (1994), Heat and water vapour fluxes and scalar roughness lengths over an Antarctic ice shelf, *Boundary Layer Meteorol.*, *69*, 101–121.
- King, J. C., and W. M. Connolley (1997), Validation of the surface energy balance over the Antarctic Ice Sheet in the U.K. Meteorological Office unified climate model, *J. Clim.*, *10*, 1273–1287.
- King, J. C., and J. Turner (1997), *Antarctic Meteorology and Climatology*, Cambridge Atmospheric and Space Science Series, Cambridge Univ. Press.
- King, J. C., W. M. Connolley, and S. H. Derbyshire (2001), Sensitivity of modelled Antarctic climate to surface and boundary-layer flux parametrizations, *Q. J. R. Meteorol. Soc.*, *127*, 779–794.
- King, J. C., S. A. Argentini, and P. S. Anderson (2006), Contrasts between the summertime surface energy balance and boundary layer structure at Dome C and Halley stations, Antarctica, *J. Geophys. Res.*, *111*, D02105, doi:10.1029/2005JD006130.
- King, J. C., A. Jrrar, and W. M. Connolley (2007), Sensitivity of modelled atmospheric circulation to the representation of stable boundary layer processes, *Geophys. Res. Lett.*, *34*, L06708, doi:10.1029/2006GL028563.
- Krinner, G., C. Genthon, Z.-X. Li, and P. Le Van (1997), Studies of the Antarctic climate with a stretched-grid general circulation model, *J. Geophys. Res.*, *102*(D12), 13,731–13,745.
- Krinner, G., C. Largeron, M. Ménéguez, C. Agosta, and C. Brutel-Vuilmet (2014), Oceanic forcing of Antarctic climate change: A study using a stretched-grid atmospheric general circulation model, *J. Clim.*, *27*, 5786–5800, doi:10.1175/JCLI-D-13-00367.1.
- Lanconelli, C., M. Busetto, E. G. Dutton, G. König-Langlo, M. Maturilli, R. Sieger, V. Vitale, and T. Yamanouchi (2011), Polar baseline surface radiation measurements during the international polar year 2007–2009, *Earth Syst. Sci. Data Discuss.*, *3*, 1–8, doi:10.5194/essd-3-1-2011.
- Libois, Q., G. Picard, L. Arnaud, S. Morin, and E. Brun (2014), Modeling the impact of snow drift on the decimeter-scale variability of snow properties on the Antarctic Plateau, *J. Geophys. Res. Atmos.*, *119*, 662–681, doi:10.1002/2014JD022361.
- Louis, J. F., M. Tiedtke, and J.-F. Geleyn (1982), A short history of the operational PBL parameterization at ECMWF, paper presented at the ECMWF Workshop on Boundary Layer Parametrization, November 1981, ECMWF, Reading, U. K.

- Mahrt, L. (1987), Grid-averaged surface fluxes, *Mon. Weather Rev.*, *115*, 1550–1560.
- Mahrt, L. (2014), Stably stratified atmospheric boundary layers, *Annu. Rev. Fluid Mech.*, *46*, 23–45, doi:10.1146/annurev-fluid-010313-14135.
- Mauritsen, T., G. Svensson, S. Zilitinkevich, I. Esau, L. Enger, and B. Grisogono (2007), A total turbulent energy closure model for neutrally and stably stratified atmospheric boundary layers, *J. Atmos. Sci.*, *64*, 4113–4125, doi:10.1175/2007JAS2294.1.
- McNider, R. T., G. J. Steeneveld, A. A. M. Holtslag, R. A. Pielke Sr., S. Mackaro, A. Pour-Biazar, J. Walters, U. Nair, and J. Christy (2012), Response and sensitivity of the nocturnal boundary layer over land to added longwave radiative forcing, *J. Geophys. Res.*, *117*, D14106, doi:10.1029/2012JD017578.
- Mellor, G. L., and T. Yamada (1974), A hierarchy of turbulence closure models for planetary boundary layers, *J. Atmos. Sci.*, *30*, 1061–1069.
- Mellor, G. L., and T. Yamada (1982), Development of a turbulence closure model for geophysical fluid problems, *Rev. Geophys.*, *20*(4), 851–875.
- Mirocha, J. D., and B. Kosović (2010), A large-eddy simulation study of the influence of subsidence on the stably stratified atmospheric boundary layer, *Boundary Layer Meteorol.*, *134*(1), 1, doi:10.1007/s10546-009-9449-4.
- Morcrette, J.-J., L. Smith, and Y. Fouquart (1986), Pressure and temperature dependence of the absorption in longwave radiation parametrizations, *Contrib. Atmos. Phys.*, *59*(4), 455–469.
- Morcrette, J.-J., E. J. Mlawer, M. J. Iacono, and S. A. Clough (2001), Impact of the radiation-transfer scheme RRTM in the ECMWF forecasting system, *Eur. Centre Medium-Range Weather Forecasts Newsl.*, *91*, 2–9.
- Parish, T. R., and D. H. Bromwich (1987), The surface windfield over the Antarctic ice sheets, *Nature*, *328*, 51–54.
- Pietroni, I., S. Argentini, I. Petenko, and R. Sozzi (2012), Measurements and parametrizations of the atmospheric boundary-layer height at Dome C, Antarctica, *Boundary Layer Meteorol.*, *143*, 189–206, doi:10.1007/s10546-011-9675-4.
- Rio, C., F. Hourdin, F. Couvreux, and A. Jam (2010), Resolved versus parametrized boundary-layer plumes. Part II: Continuous formulations of mixing rates for mass-flux schemes, *Boundary Layer Meteorol.*, *135*, 469–483, doi:10.1007/s10546-010-9478.
- Sandu, I., A. Beljaars, P. Bechtold, T. Mauritsen, and G. Balsamo (2013), Why is it so difficult to represent stably stratified conditions in Numerical Weather Prediction (NWP) models, *J. Adv. Model Earth Syst.*, *5*, 117–133, doi:10.1002/jame.20013.
- Scheider, D. P., and D. B. Reush (2016), Antarctic and Southern Ocean surface temperatures in CMIP5 models in the context of the surface energy budget, *J. Clim.*, *29*, 1689–1716, doi:10.1175/JCLI-D-15-0429.1.
- Steenefeld, G. J., A. A. M. Holtslag, C. J. Nappo, B. J. H. van de Wiel, and L. Mahrt (2008), Exploring the possible role of small-scale terrain drag on stable boundary layers over land, *J. Appl. Meteorol. Climatol.*, *47*(10), 2518–2530, doi:10.1175/2008JAMC1816.1.
- Steenefeld, G. J., M. J. J. Wokke, C. D. Groot Zwaafink, S. Pijlman, B. G. Heusinkveld, A. F. G. Jacobs, and A. A. M. Holtslag (2010), Observations of the radiation divergence in the surface layer and its implication for its parametrization in numerical weather prediction models, *J. Geophys. Res.*, *115*, D06107, doi:10.1029/2009JD013074.
- Sterk, H. A. M., G. J. Steeneveld, and A. A. M. Holtslag (2013), The role of snow-surface coupling, radiation, and turbulent mixing in modeling a stable boundary layer over Arctic sea ice, *J. Geophys. Res. Atmos.*, *118*, 1199–1217, doi:10.1002/jgrd.50158.
- Sterk, H. A. M., G. J. Steeneveld, T. Vihma, P. S. Anderson, F. C. Bosveld, and A. A. M. Holtslag (2015), Clear-sky stable boundary layers with low winds over snow-covered surfaces. Part 1: WRF model evaluation, *Q. J. R. Meteorol. Soc.*, *141*(691), 2165–2184, doi:10.1002/qj.2513.
- Sterk, H. A. M., G. J. Steeneveld, F. C. Bosveld, T. Vihma, P. S. Anderson, and A. A. M. Holtslag (2016), Clear-sky stable boundary layers with low winds over snow-covered surfaces. Part 2: Process sensitivity, *Q. J. R. Meteorol. Soc.*, *142*(695), 821–835, doi:10.1002/qj.2684.
- Sukoriansky, S., P. Galperin, and P. Veniamin (2005), Application of a new spectral theory on stably stratified turbulence to the atmospheric boundary layer over sea ice, *Boundary Layer Meteorol.*, *117*, 231–257.
- Svensson, G., and J. Lindvall (2015), Evaluation of near-surface variables and the vertical structure of the boundary layer in CMIP5 models, *J. Clim.*, *28*(13), 5233–5253, doi:10.1175/JCLI-D-14-00596.1.
- Svensson, G., et al. (2011), Evaluation of the diurnal cycle in the atmospheric boundary layer over land as represented by a variety of single-column models: The second GABLS experiment, *Boundary Layer Meteorol.*, *140*(2), 177–206, doi:10.1007/s10546-011-9611-7.
- Town, M., V. P. Walden, and S. G. Warren (2005), Spectral and broadband longwave downwelling radiative fluxes, cloud radiative forcing and fractional cloud cover over the South Pole, *J. Clim.*, *18*, 4235–4252.
- van de Wiel, B. J. H., A. F. Moene, G. J. Steeneveld, P. Baas, F. C. Bosveld, and A. A. M. Holtslag (2010), A conceptual view on inertial oscillations and nocturnal low-level jets, *J. Atmos. Sci.*, *67*, 2679–2689, doi:10.1175/2010JAS3289.1.
- van de Wiel, B. J. H., E. Vignon, P. Baas, I. G. S. van Hooijdonk, S. J. A. van der Linden, J. A. van Hooft, F. C. Bosveld, S. R. de Roode, A. F. Moene, and C. Genthon (2017), Regime transition in near-surface temperature inversions: A conceptual model, *J. Atmos. Sci.*, *74*, 1057–1073, doi:10.1175/JAS-D-16-0180.1.
- Vignon, E., C. Genthon, H. Barral, C. Amory, G. Picard, H. Gallée, G. Casasanta, and S. Argentini (2016), Momentum and heat flux parametrization at Dome C, Antarctica: A sensitivity study, *Boundary Layer Meteorol.*, *162*(2), 341–367, doi:10.1007/s10546-016-0192-3.
- Vignon, E., B. J. H. van de Wiel, I. G. S. van Hooijdonk, C. Genthon, S. J. A. van der Linden, J. A. van Hooft, P. Baas, W. Maurel, O. Traullé, and G. Casasanta (2017), Stable boundary-layer regimes at Dome C, Antarctica: Observation and analysis, *Q. J. R. Meteorol. Soc.*, *143*, 1241–1253, doi:10.1002/qj.2998.
- Viterbo, P., A. Beljaars, J. F. Mahfouf, and J. Teixeira (1999), The representation of soil moisture freezing and its impact on the stable boundary layer, *Q. J. R. Meteorol. Soc.*, *125*, 2401–2426.
- Walters, J. T., R. T. McNider, X. Shi, W. B. Norris, and J. R. Christy (2007), Positive surface temperature feedback in the stable nocturnal boundary layer, *Geophys. Res. Lett.*, *34*, L12709, doi:10.1029/2007GL029505.
- Wild, M., A. Ohmura, H. Gilden, J. J. Morcrette, and A. Slingo (2001), Evaluation of downward longwave radiation in general circulation models, *J. Clim.*, *14*, 3227–3239.
- Yamada, T. (1983), Simulations of nocturnal drainage flows by a  $q^2$  turbulence closure model, *J. Atmos. Sci.*, *40*, 91–106.
- Yen, Y.-C. (1981), Review of thermal properties of snow, ice and sea ice, United States Army Corps of Engineers, Hanover, N. H., USACRREL Rep. 81-10, pp. 1–27.
- Zilitinkevich, S., T. Elperin, N. Kleeorin, and I. Rogachevskii (2007), Energy- and flux-budget turbulence closure model for stably stratified flows. Part I: Steady state, homogeneous regime, *Boundary Layer Meteorol.*, *125*, 167–191, doi:10.1007/s10546-007-9189-2.
- Zilitinkevich, S., T. Elperin, N. Kleeorin, I. Rogachevskii, I. Esau, T. Mauritsen, and M. W. Miles (2008), Turbulence energetics in stably stratified geophysical flows: Strong and weak mixing regimes, *Q. J. R. Meteorol. Soc.*, *134*, 793–799, doi:10.1002/qj.264.
- Zilitinkevich, S., T. Elperin, N. Kleeorin, I. Rogachevskii, and I. Esau (2013), A hierarchy of Energy- and Flux-Budget (EFB) turbulence closure models for stably-stratified geophysical flows, *Boundary Layer Meteorol.*, *146*, 341–373, doi:10.1007/s10546-012-9768-8.